AN OVERVIEW OF THE INSTRUMENT SUITE FOR THE DEEP IMPACT MISSION

DONALD L. HAMPTON[1,*], JAMES W. BAER[1], MARTIN A. HUISJEN[1],
CHRIS C. VARNER[1], ALAN DELAMERE[1], DENNIS D. WELLNITZ[2],
MICHAEL F. A'HEARN[2] and KENNETH P. KLAASEN[3]

[1]*Ball Aerospace & Technologies Corporation, P.O. Box 1062, Boulder, CO 80301, U.S.A.*
[2]*Department of Astronomy, University of Maryland, College Park, MD 20742-2421, U.S.A.*
[3]*Jet Propulsion Laboratory, California Institute of Technology, 4800 Oak Grove Drive,
Pasadena, CA 91109, U.S.A.*
(*Author for correspondence; E-mail: dhampton@ball.com)

Abstract. A suite of three optical instruments has been developed to observe Comet 9P/Tempel 1, the impact of a dedicated impactor spacecraft, and the resulting crater formation for the Deep Impact mission. The high-resolution instrument (HRI) consists of an $f/35$ telescope with 10.5 m focal length, and a combined filtered CCD camera and IR spectrometer. The medium-resolution instrument (MRI) consists of an $f/17.5$ telescope with a 2.1 m focal length feeding a filtered CCD camera. The HRI and MRI are mounted on an instrument platform on the flyby spacecraft, along with the spacecraft star trackers and inertial reference unit. The third instrument is a simple unfiltered CCD camera with the same telescope as MRI, mounted within the impactor spacecraft. All three instruments use a Fairchild split-frame-transfer CCD with $1,024 \times 1,024$ active pixels. The IR spectrometer is a two-prism (CaF_2 and ZnSe) imaging spectrometer imaged on a Rockwell HAWAII-1R HgCdTe MWIR array. The CCDs and IR FPA are read out and digitized to 14 bits by a set of dedicated instrument electronics, one set per instrument. Each electronics box is controlled by a radiation-hard TSC695F microprocessor. Software running on the microprocessor executes imaging commands from a sequence engine on the spacecraft. Commands and telemetry are transmitted *via* a MIL-STD-1553 interface, while image data are transmitted to the spacecraft *via* a low-voltage differential signaling (LVDS) interface standard. The instruments are used as the science instruments and are used for the optical navigation of both spacecraft. This paper presents an overview of the instrument suite designs, functionality, calibration and operational considerations.

Keywords: comets, CCD cameras, IR spectrometer

Abbreviations: A/D – analog to digital converter; CCD – charge coupled device; DAC – digital to analog converter; DN – digital number (or data number); EEPROM – electrically erasable programmable read-only memory; FPA – focal plane array; FPGA – field programmable gate array; FWHM – full width at half maximum; HRI – high-resolution instrument; IC – instrument controller; ICB – instrument and impactor crosslink board; IP – instrument platform; IR – infrared; IRS – (Spitzer) infrared spectrograph; ITC – instrument time code; ITOC – Instrument Test and Operations Console; ITS – impactor targeting sensor; LVDS – low-voltage differential signaling; LVPS – low voltage power supply; MIPS – multiband imaging photometer for Spitzer; MRI – medium-resolution instrument; MSSRD – Mission, Science, and Systems Requirements Document; MTLM – mechanism and telemetry board; MWIR – mid-wave infrared; NVM – non-volatile memory; PROM – programmable read-only memory; PSF – point spread function; QE – quantum efficiency; S/C – spacecraft; SCU – spacecraft control unit; SIM – spectral imaging module; SNR – signal to noise ratio; SRAM – static

random access memory; TPG – timing pattern generator; TVAC – thermal vacuum (test); VME – Versa Module Europa (IEEE 1014-1987 standard); VTC – vehicle time code

1. Introduction

The NASA Deep Impact mission is designed to deliver an impactor spacecraft with a mass of about 360 kg to collide with comet Tempel 1 in early July 2005, at a relative speed of approximately 10 km/s. The impactor and flyby spacecraft are launched attached to one another and separate about 24 h before impact. The flyby spacecraft diverts and slows down to fly by the nucleus at a range of 500 km, at about 14 min after the impact. The goal of the impact is to create an impact crater in the surface of the comet and to expose pristine material underneath the nuclear crust to be observed by the flyby. Minimal knowledge of the physical properties of the surfaces and interiors of cometary nuclei results in a large range of possible ejecta plumes and crater depths and diameters. This mission is truly an experiment and almost any observable outcome will significantly improve our knowledge of the properties of cometary nuclei. The challenge in the design of the instruments is to be able to get useful data for any outcome within the range of possibilities.

The Deep Impact scientific suite consists of three optical instruments: a high-resolution instrument (HRI) and a medium-resolution instrument (MRI) on the flyby spacecraft, and an impactor targeting sensor (ITS), mounted on the impactor. The HRI incorporates a 30-cm aperture, 10.5-m focal length telescope feeding both a filtered CCD camera covering the wavelength range from 0.32 (at 50% transmission) to 1.05 μm ("visible light") and a long-slit IR spectrometer with spectral range from 1.05 to 4.8 μm. The MRI incorporates a 12-cm aperture, 2.1-m focal length telescope that feeds a filtered visible-light CCD camera. The ITS telescope is identical to the MRI telescope, but feeds an unfiltered CCD camera. Table I summarizes the physical attributes of the instruments.

Figure 1 shows the block diagram of the HRI, and Figure 2 shows the block diagram of the MRI or ITS, which are identical, except for the inclusion or exclusion of the filter wheel.

The detectors and mechanisms are controlled with a set of dedicated instrument electronics – one for each instrument. These electronics are controlled by commands *via* a MIL-STD-1553 interface. Health and status telemetry from the instruments also are transmitted to the spacecraft *via* this interface. Image data are transmitted to the spacecraft *via* a dedicated low-voltage differential signaling (LVDS) interface, as shown in both Figures 1 and 2.

In this paper, we describe the mission objectives and how these translated into requirements on the instruments. We then describe the design of the instruments from optical and mechanical through electronics and software. We then describe the instrument imaging modes and the data flow from the instruments to the Deep Impact spacecraft. The integration and test of the instruments is described along

TABLE I

Instrument optical summary.

	HRI	MRI	ITS
Telescopes			
Diameter (cm)	30	12	12
Focal length (m)	10.5	2.1	2.1
$f/\#$	35	17.5	17.5
Visible			
Format	1,024 × 1,024 split frame transfer CCD		
Pixel size (μm)	21	21	21
IFOV (m-rad)	2.0	10.0	10.0
FOV (mrad)	2.0	10.0	10.0
FOV (°)	0.118	0.587	0.587
Scale per pixel (m)	1.4 at 700 km	7 at 700 km	0.2 at 20 km
IR			
Format	512 × 256 HgCdTe FPA[a]		
Pixel size (μm)	36		
Spatial			
IFOV (μ-rad)	10.0		
FOV (mrad)	2.5		
FOV (°)	0.15		
Spectral			
IFOV (μ-rad)	10.0		
FOV (μ-rad) (slit width)	10.0		
Spectral range	1.05–4.8 μm		
Minimum $\lambda/d\lambda$	216		

[a] 1,024 × 512 rebinned 2 × 2.

with the results of that testing. Finally, some operational considerations for the instruments are presented.

2. Requirements and Mission Objectives

The general mission objectives are discussed by A'Hearn *et al.* elsewhere in this issue. From the general mission objectives it was possible to derive a set of requirements for the capabilities of the instruments. However, the uncertainty about which physics is relevant to the impact and thus about what will be observable, led to necessary compromises in the requirements. The resulting requirements were thus
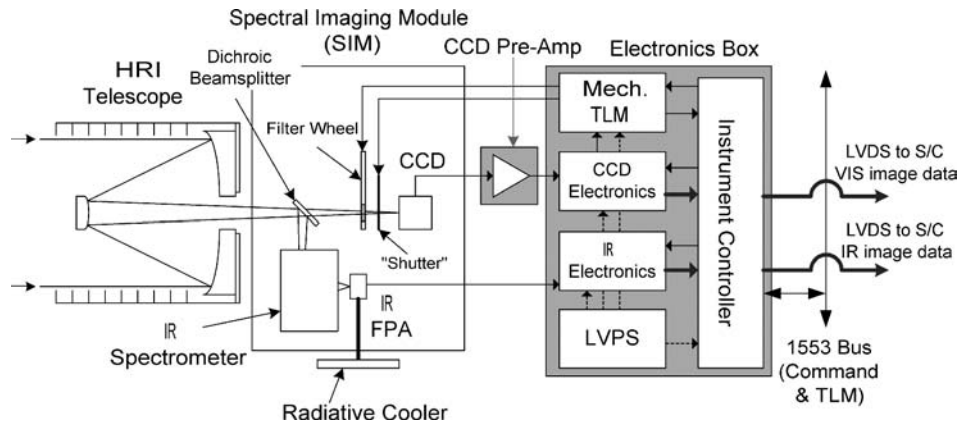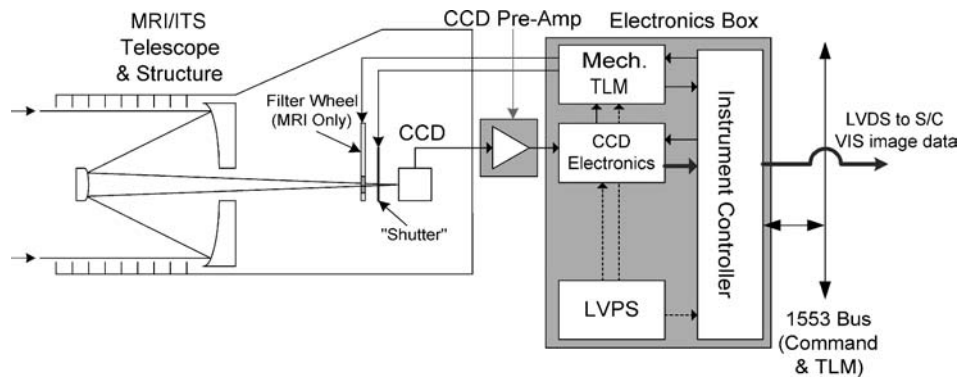
Figure 1. HRI block diagram.

Figure 2. MRI/ITS block diagram.

targeted at the baseline scenario (see article by A'Hearn *et al.*, Schultz *et al.*, and Melosh *et al.*, in this issue) but intended to ensure that the mission would still return useful information in the event that the baseline assumptions are not correct. As examples, crater formation could be considerably slower than assumed, by as much as a factor of 3; the crater depth could vary from the baseline assumption by a factor of 2; and the diameter of the crater could be as little as 2 m or as large as 200 m according to various models. The requirements have been codified in the Mission, Science, and Systems Requirements Document (MSSRD). Cost restrictions have resulted in de-scopes from the originally proposed instruments. In this description, we will use the current version of the MSSRD (Revision C, 2004), which incorporates all de-scopes to date. The requirements on the instruments derive directly from Section 3.2 "Science Observational Requirements", which is reproduced, in part, later. The MSSRD document defines the albedo, phase function, phase angle and range from the sun that are the baseline values accepted by the science team. These values are implicit in the following requirements.

The following observational requirements assume that pointing accuracy is sufficient to avoid the need for (mosaic imaging maneuvers) and that pointing has recovered from any previous dust impacts.

1. Optical images shall be obtained showing growth of the impact crater and the ejecta cone, including, if possible, bright ejecta emanating from the impact.
2. IR spectra shall be obtained of the down-range ejecta near the crater.
3. At least 660 s (three times the baseline prediction for crater formation time) shall be used to observe the crater growth, to allow for uncertainties in the predicted phenomena.
4. The instruments shall perform visible and infrared observations of the comet, as follows: (a) visible imaging shall cover the spectral range from 0.3 to 0.95 μm; (b) infrared spectroscopic imaging shall cover the spectral range from 1.05 to 4.8 μm.
5. The instruments shall observe comet brightness variations due to rotation prior to its being spatially resolved, plus the natural comet shape and surface features before and after impact, and after orbit plane crossing.
6. A sequence of pre-impact images from the impactor of the surface, including a context image of the predicted crater location, shall be obtained with the following image scales and fields of view:

Observation	Image scale	Field of view (minimum)
Nucleus w/coma	30 m/pixel	15×15 km
Full nucleus	10 m/pixel	2.5×2.5 km
Impact target area	1.5 m/pixel	180×180 m
Target point	0.6 m/pixel	30×30 m

7. The ejecta cloud, including the inner coma up to two times the nucleus' radius above the surface, shall be observed, in the visible range, at a pixel scale of 25 m or less, with an SNR of ≥ 30.
8. The fully developed crater shall be observed in the visible range,

   (a) at <3.4 m total resolution (i.e. system point spread function (PSF), full width half max) with an SNR of ≥ 70 and
   (b) at <5.5 m total resolution with an SNR of ≥ 100, using no filter in either case, all with a field of view of >360 m (three times the predicted crater diameter).

9. The fully developed crater shall be observed in the visible range using geology filters at <6 m total resolution with an SNR of ≥ 50, with a >360 m FOV.
10. The crater shall be observed spectrally (across the IR wavelength range) at a spectral resolving power ≥ 200 and at spatial resolution of <25 m.
11. The entire comet shall be observed spectrally (across the IR wavelength range) at a spectral resolving power ≥ 200 and at spatial resolution of <130 m.

12. An IR spectrum of ejecta and outgassing in the area of the down-range limb shall be obtained in the 1.05–4.8 μm wavelength range after impact.
13. To provide area context, near-simultaneous visible observations shall be taken with five times the field of view of the high-resolution instrument.
14. To facilitate analysis, a complete set of pre-impact context observations shall be obtained as close to the time of impact as practical of the impact point (visible and IR), the down-range limb area (IR only), and the inner coma (visible only).
15. The SNR for visible global imaging of the comet for the expected geometric albedo (4%) and phase function (value = 0.0135) and a phase angle of $<70°$ shall be ≥ 250 for broadband nucleus observations and ≥ 100 when observing the nucleus using geology filters.
16. The minimum SNR for IR observations of the comet nucleus (averaged over the illuminated portion of the nucleus) in the 1.05–4.8 μm range for the expected reflectivity (4%) and a phase angle of $<70°$ shall be ≥ 50.
17. The visible and IR imaging shall have spatial, sensitivity, and spectral characteristics that are capable of achieving the science goals at the assumed comet albedo and the illumination angles planned for the mission.
18. The performance for visible imaging of the cometary coma, for expected brightness (of 0.3 ergs/cm^2/s/sr over a bandpass from 520 to 540 nm) and a phase angle $<70°$ shall (a) provide an SNR greater than or equal to 100 when observing the coma using dust (or geology) filters and (b) ensure a digitized signal level that is at least 2 DN (data numbers) higher than background when observing comet pre-impact gas emissions with gas emission filters.

3. Instrument Design

Translating the scientific observation requirements into instrument designs was accomplished by engineers at Ball Aerospace & Technologies Corporation, working to the requirements as set forth in the MSSRD and as translated by the systems engineers into more detailed "Level B Specifications". The approach, as described in the initial proposal and as it exists today (less de-scopes described later) was to have one visible camera system, called the ITS, on the impactor spacecraft and two instruments on the flyby spacecraft. This array of instruments would provide the scientific observations and also be used for autonavigation of the two spacecrafts.

Having two instruments on the flyby spacecraft provides some redundancy as well as some capability for optimization of the two instruments for different types of observations. The HRI incorporates both an infrared imaging spectrometer and a visible imaging camera with a wheel of nine filters optimized for surface characterization, while the MRI incorporates only a visible imaging camera, also with nine filters, including some optimized for coma studies and some identical with those in the HRI. Both instruments are mounted to an instrument platform, which also holds two star trackers and the inertial reference unit, maintaining all of these

in fixed alignment with respect to each other independent of distortion in the body of the flyby spacecraft.

A planned, second infrared spectrometer on the MRI was eliminated in a descope. Similarly, the planned ability to scan the infrared spectrometer slit over the field of view of the HRI visible imager was eliminated in another de-scope; the spectrometer slit currently has a fixed location in the HRI field of view, so scanning the slit over the nucleus of the comet is accomplished by rotation of the entire spacecraft.

3.1. OPTICAL AND MECHANICAL

The parameters of the mission (flyby velocity and distance, desired resolution and fields of view, expected coma brightness, nucleus albedo and phase function, desired time resolution for impact and crater formation, and so on) constrain the design of the instruments. Within these constraints, we attempted to minimize design effort and enhance manufacturability to keep costs acceptable. Therefore, the ITS and MRI were designed to use identical telescopes, all visible sensors were designed to use identical CCDs, both MRI and HRI were designed to use identical filter wheels (but with different filters in the wheels), and all visible imagers were designed to use identical light blockers.

3.1.1. *Telescopes*

Two Cassegrain telescopes were designed for use in the Deep Impact instruments. The HRI telescope is a 30-cm aperture 10.5-m focal length optic resulting in a relatively slow $f/35$ focal ratio. Both the MRI and ITS have 12-cm apertures and 2.1-m focal lengths resulting in faster $f/17.5$ telescopes. The apertures, focal lengths, and resultant f-ratios for the telescopes were derived directly from the science requirements for resolutions, fields of view, and throughput of the visible imagers and the infrared spectrometer. The f-ratios for the primary mirrors, separations of secondary mirrors from primary mirrors, and distances from the back of the primary to focus were all determined from packaging and mounting constraints including accommodation of filter wheels, light blockers and, in the case of the HRI, the dichroic beamsplitter described later. In fact, a major driver for the HRI telescope was that it must mount on the spacecraft but not violate the envelope of the launch vehicle fairing.

The mirrors are made from Zerodur® glass ceramic, and the reflective surfaces are coated with Al with a SiO_2 overcoat for surface protection.

Because the instruments are intended to operate at low temperatures, the telescope optics were mounted on flexures within carbon composite structures having slightly negative coefficients of expansion, so that the separations of primary and secondary mirrors could be designed to remain essentially constant over large variations in structure temperature, eliminating the need for focus mechanisms. Tests of these instruments over ranges of temperature from $+60\,°C$, high above the expected
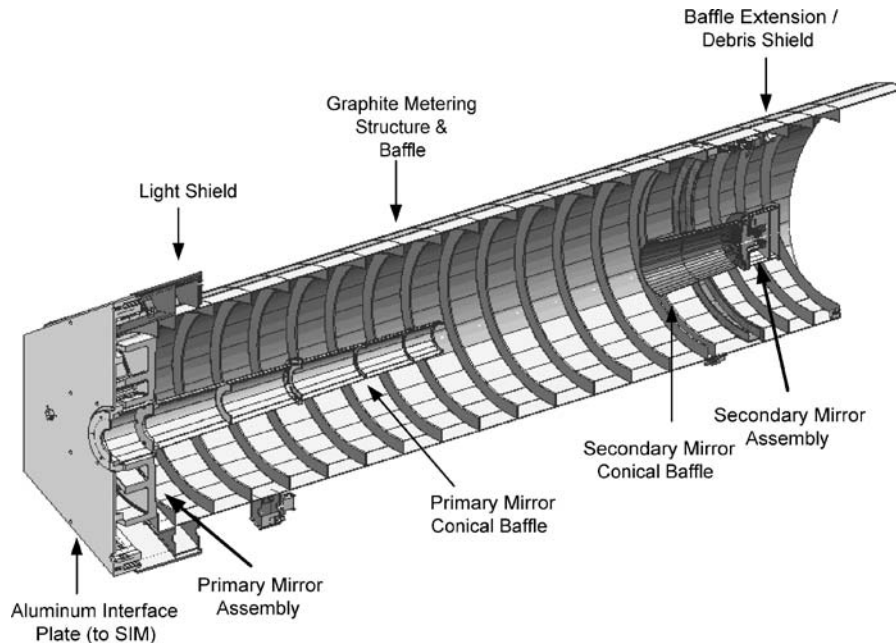
Figure 3. HRI telescope.

operating temperatures, to temperatures as low as $-170\,^{\circ}$C, close to the expected coldest operating temperature of the HRI telescope, showed that the telescopes would maintain correct focus over the ranges of their respective expected operating temperatures.

The telescopes were designed with several features to reduce stray light. In addition to including multiple internal baffles within the main telescope tube structure (see Figure 3), there are conical baffles around the outside of the secondary mirror, and within the central hole of the primary mirror. These two mirror baffles prevent any light outside of the instrument field of view from directly reaching the CCD, or the HRI IR spectrometer slit. The graphite structure that forms all of the internal telescope tube baffles typically has a normal incidence reflectivity of 15%.

3.1.2. *HRI Spectral Imaging Module*
The spectral imaging module (SIM) of the HRI incorporates both the visible detector with its associated filter wheel and light blocker and the infrared spectrometer, using a custom-designed dichroic beamsplitter to reflect the visible light and transmit the infrared. Figure 4 shows the layout of the SIM instrument.

The IR imaging spectrometer operates from 1.05 to 4.80 μm with a spectral resolving power ($\lambda/\Delta\lambda$) that varies from a minimum of 200 at middle wavelengths to higher values at shorter and longer wavelengths. The spectrometer uses prisms for dispersion and diamond-turned optics for collimating and imaging. Imaging along
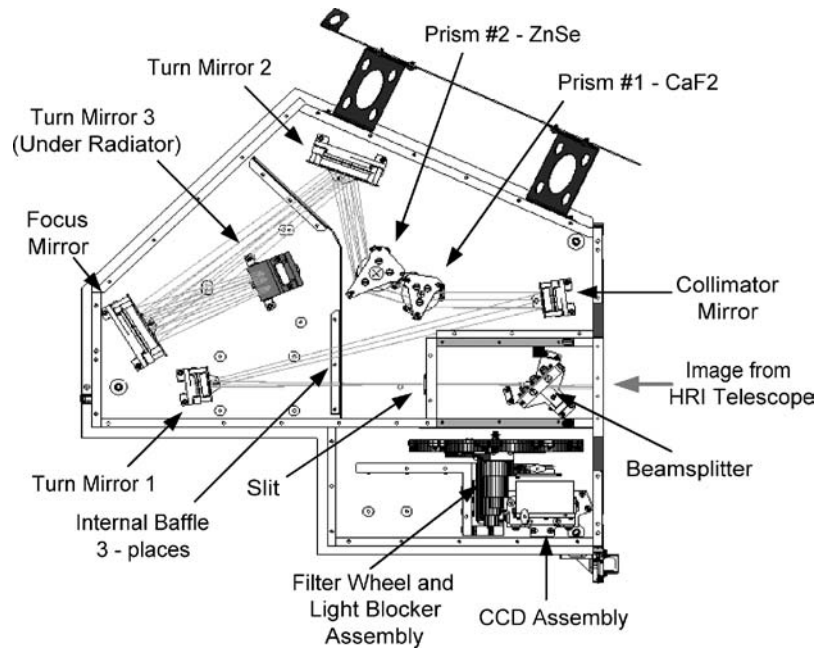
Figure 4. HRI spectral imaging module, without IR detector radiator. The structure at the top of the image is a debris shield that will protect the SIM from particle damage during the encounter.

the slit is maintained for the full 0.145° slit-length field of view. The spacecraft will rotate to scan a scene across the slit to obtain a spectral image cube.

A prism spectrometer was chosen over a more typical grating spectrometer for two reasons. First, the large spectral range (over two octaves) would require order sorting filters in a grating spectrometer, but not in a prism spectrometer. Eliminating such filters reduced the number of optics required to be mounted. Second, the large spectral range would results in a large range of spectral resolving power for a grating spectrometer. In the extreme of an ideal linear grating spectrometer, meeting the required resolving power of 200 at 1.05 μm would result in a resolving power of more than 25,000 at 4.8 μm, and require a detector with nearly 20,000 elements to cover the entire spectrum. Choosing materials with two complementing indices of refraction resulted in a relatively flat resolving power across the large wavelength range, and thus kept the spectrum at a manageable size to fit on an existing detector. The measured resolving power is shown in Figure 27, and discussed in Section 5.3.6.

After the infrared light passes through the beamsplitter and slit, a fold mirror reflects the rays onto a spherical collimator mirror. The collimated beam is refracted through a calcium fluoride (CaF_2) prism and through a zinc selenide (ZnSe) prism, reflected off another fold mirror, and then reflected by a spherical camera mirror that images the spectrum. After the camera mirror another fold mirror, "Turn Mirror #3" in the figure, reflects the light out of the plane of the figure and onto the IR detector.

The reason for the out-of-plane reflection is to permit the use of a radiative cooler, attached to the back of the IR detector, viewing radiatively cold open space. An impressive part of the optical design is the incorporation of an aspherical surface on the exit face of the ZnSe prism, which acts as a Schmidt corrector for the spherical camera mirror providing, without the use of additional optical surfaces, the large field of view required for accurate imaging of the entire length of the slit.

Other than the prisms, beamsplitter, and detector all components of the IR spectrometer are aluminum. The optical bench is made of honeycomb aluminum with bonded aluminum face sheets. Mounting points in the optical bench for optics and side walls are aluminum inserts. The sides and top cover are all machined aluminum. The reflective optics are diamond-turned aluminum, mated to aluminum optics mounts. The prisms and beamsplitter are mounted within aluminum frames *via* spring-loaded plastic pads that maintain tension at room temperature so that the prisms survive the launch environment, and take up tension as the aluminum frames contract. The mounting of the IR detector to its two-stage radiative cooler is described in Section 3.2.3. Without the prisms, the all-aluminum optical design would be largely a-thermal. The prisms have different thermal expansion characteristics, and the index of refraction of the CaF_2 and ZnSe also change with temperature (Tropf, 1995)

The requirements to observe both the comet nucleus and the coma (see Section 2, numbers 11, 12, 13, and 15), resulted in a dynamic range that could not be accommodated by the single IR detector. The sub-solar point on the nucleus could be as warm as 300 K (Lisse, personal communication, 2003), while CO emission lines at 4.6 and 4.7 μm could be as dim as 100 kilo-Rayleighs. This results in a ratio of 1:10,000 in brightness. The problem is due mostly to the warm nucleus producing a high flux at the long-wavelength end of the spectrometer that will saturate the detector in the minimum full-frame exposure (2.9 s). Therefore, a spectral attenuator was added at the entrance slit that reduces the long wavelength flux over half the slit length. The filter is a made of polished, 1.0-mm thick, Schott WG 295 glass. The spectral characteristics are shown in Figure 5. The filter is arranged to cover the middle third of the slit, so that the top and bottom thirds are un-filtered. Since the imaging sequence will place the nucleus in the center of the IR detector, the filter arrangement will attenuate the warm nucleus signal while not filtering the low signal coma gas and dust. During the last minutes of the encounter, the nucleus may extend beyond the filter, and the long wavelength measurements may saturate. However, unlike the CCD (see Section 3.3.1), the saturated signal does not bleed across the array, and the spectrum below 3.5 μm should not be affected.

The beamsplitter reflects light in the visible band to the HRI CCD, and transmits light in the IR band to the slit of the IR spectrometer. The requirements on the beamsplitter were quite stringent with a precise 1.05-μm crossover and providing high-efficiency transmission over more than two octaves of IR wavelength, and high reflectivity from 0.34 to 1.05 μm. Figure 6 shows the resulting reflectivity and transmission. The crossover point is well positioned at 1.05 μm.
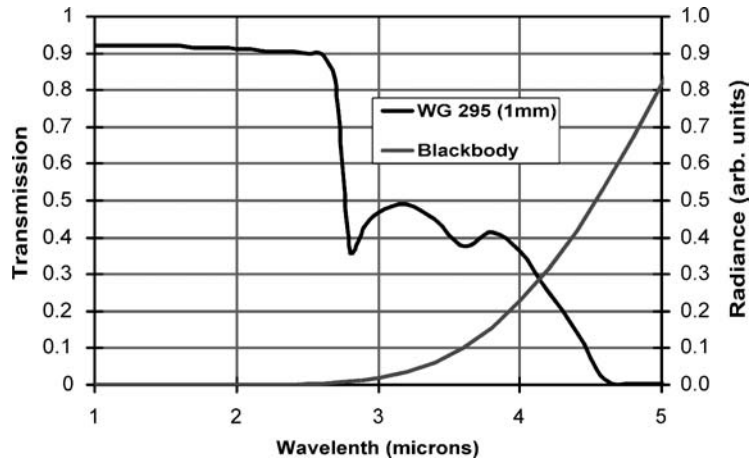
Figure 5. Transmission of the IR attenuator filter. The filter is made of 1-mm thick Schott WG 295 glass. Also shown is the radiance of a 300 K blackbody showing how quickly the brightness changes with wavelength at 3–5 μm. Portions of the comet nucleus surface may be as warm as 290 K.
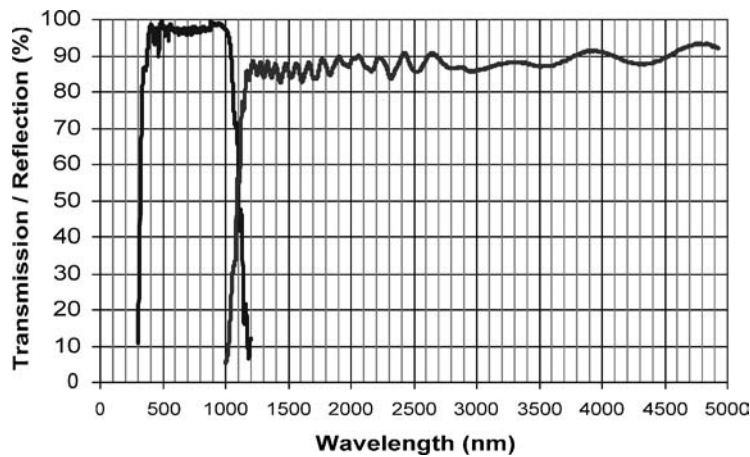

Figure 6. HRI beamsplitter optical properties. The darker profile on the left is visible reflectivity, the lighter profile is the IR transmission.

3.1.3. *Mechanisms*

3.1.3.1. Filter Wheel. Figure 7 shows the 9-in. diameter HRI filter wheel with its nine optical filters spaced at 40° intervals. The MRI filter wheel design is identical except for the mounting brackets. The filter cells are separate and complete assemblies that mount into the magnesium wheel. Both filter wheels are required to move between adjacent filter positions within 2.2 s. The filter wheel mounts directly to the output shaft of the stepper motor gearhead. All lubricated and moving components are contained within the motor and gearhead assembly.
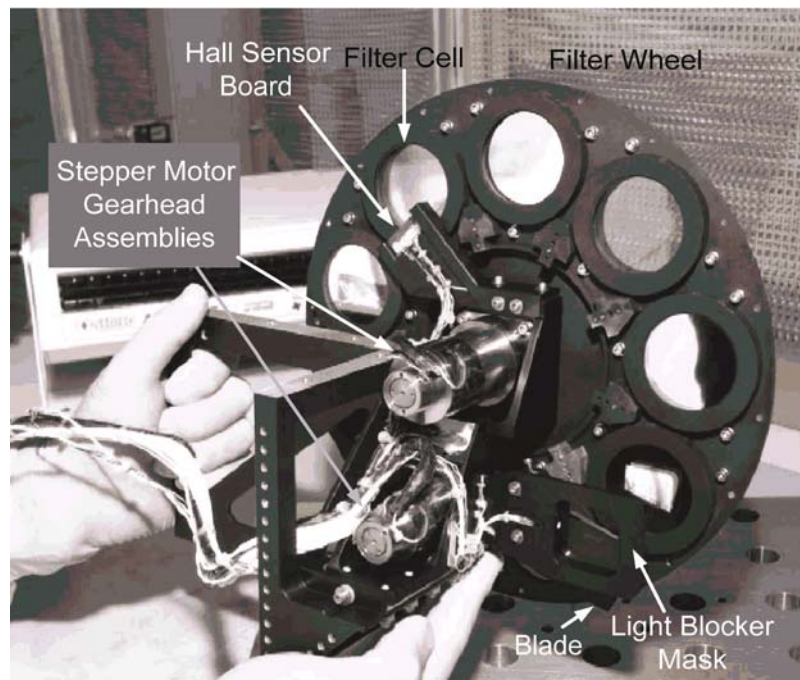
Figure 7. HRI filter wheel and light blocker.

The motor is a 30° two-phase stepper motor which, with a 96:1 gearhead ratio. It rotates the filter wheel 0.3125° per motor step so that 128 steps are required to rotate the 40° between adjacent filter positions. There are mechanical stops at filter positions 1 and 9 that limit the wheel rotation to a total of 320°. A command that causes the filter wheel to bump against a stop causes no harm to the motor or mechanism.

During normal operations, the motor is driven at 120 steps per second with 60% of the maximum possible drive current to the motor, which provides sufficient torque and inertia margin to move the wheel at the required rate. The instrument controller (IC) can directly set the mechanism Field Programmable Gate Array (FPGA) registers that control the motor pulse rate and the current drive level to the motor (0, 19, 60, and 100% of maximum).

The wheel is moved by an absolute filter position command from the spacecraft to the IC. The IC in turn sends a command to the motor control FPGA (on the mechanism and telemetry (MTLM) board) to move the desired number of steps in the correct direction. A homing command to the IC will move the wheel from any position to the clear filter in position 1. Four Hall-effects sensors provide 4-bit absolute position indication to FPGA registers that are read by the IC. Note that the wheel is moved by open-loop step commands, and the Hall sensors are used only for position confirmation. The main reason for providing absolute position indication

is to allow relatively quick resumption of critical sequence imaging following an unplanned reboot of the IC.

On initialization of the instruments, the software will check the 4-bit Hall sensor reading. For a known reading, the software will store the current measured position and consider the filter wheel initialized and proceed with executing commands. If the 4-bit Hall-effects sensors do not match a known code, then the software will begin stepping the filter wheel toward the home position (filter 1). At each step, the software will read the Hall-effects sensors and compare it to the known filter position codes. When a Hall sensor pattern that matches a known code is received, the software then sweeps several steps on either side of that position and records the Hall-effects sensor pattern at each step. The software then uses an optimization routine to determine the most central position for that code and moves the filter wheel to that position. It then stores the current position and considers the filter wheel initialized, and will proceed with executing commands. This initialization sequence takes 3 s or less, depending on where the filter wheel starts. This initialization sequence can also be commanded at any time the instrument software is in the operate state.

Table II shows the filter parameters for each filter in the HRI and MRI filter wheels, and Figure 8 shows the measured filter transmission for each filter.

Other than filter positions 1 and 6, each filter cell is made of two pieces of glass. One is a fused silica substrate on which the interference filter is deposited, while the other is a longpass or shortpass blocking filter to reduce the throughput of resonance transmission bands in the bandpass filter. The thickness of both pieces

TABLE II
Filter wheel filter characteristics filter.

Filter wheel position	MRI center (nm)	MRI filter width (nm)	MRI filter target measurement	HRI center (nm)	HRI filter width (nm)
1	650	>700[a]	Context	650	>700[a]
2	514	11.8	C_2 in coma	450	100
3	526	5.6	Dust in coma	550	100
4	750	100	Context	350	100[b]
5	950	100[c]	Context	950	100[c]
6	650	>700[a]	Context	650	>700[a]
7	387	6.2	CN in coma	750	100
8	345	6.8	Dust in coma	850	100
9	309	6.2	OH in coma	650	100

[a]Filters in positions 1 and 6 are uncoated and not band limited.
[b]The coating on the 350-nm filter is shortpass, the substrate limits the short wavelength throughput.
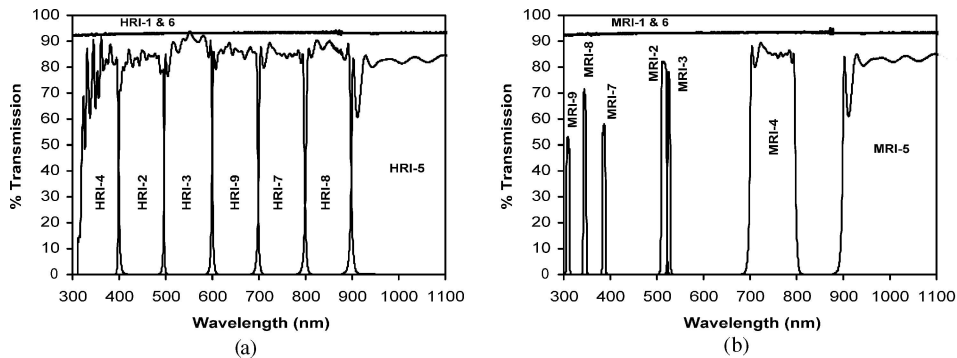[c]The 950-nm filter is longpass.

Figure 8. HRI and MRI filter transmissions. The labels refer to the filter position in the filter wheel (see Table II).

of glass in each filter cell was designed to maintain a constant optical thickness for all filter positions, and therefore maintain the same focus at all filter wheel positions.

3.1.3.2. Light Blocker. The light blocker is used in all three instruments, and acts to cover the CCD aperture between exposures. Note that we refer to this mechanism as a light blocker rather than a shutter. The length of a visible exposure is set by the start of the CCD frame transfer (see Section 3.3.1), not by the closing of a light blocker. The light blocker is used to limit the amount of light falling on the light-sensitive parts of the CCD during readout of an image; if the light were not limited during the relatively long readout times of full-frame or near-full-frame images, the light-sensitive part of the CCD could be saturated and bleed signal charge into the frame-storage area, corrupting the image.

As such, the light blocker is required to cover the aperture within 0.1 s of the end of an exposure and open within 0.2 s of the beginning of an exposure command. The light blocker mechanism is illustrated in Figure 7.

A common mounting interface is used for the light blocker in all three instruments. The blade mounts directly to the output shaft of the stepper motor gearhead. All lubricated and moving components are contained within the motor and gearhead assembly. The motor is a 30° two-phase stepper motor. The gearhead rotates the light blocker 3° per motor step, so that 12 steps are required to rotate the 36° between the "open" and "closed" positions. Mechanical stops at both ends limit the rotation of the light blocker. Single Hall-effects sensors at both ends of travel are used to sense permanent magnets mounted in the shutter, to give an indication of light blocker position. The light blocker may be moved by open-loop commands to move a number of motor steps, and the Hall sensors are used only for position confirmation. No damage to the motor or mechanism is caused by driving the light blocker against a stop.

In normal operation, the light blocker is opened and closed under control of the CCD timing pattern generator (TPG) FPGA that also controls the clock signals that drive the CCD readout. The IC can directly set the mechanism FPGA registers that control the motor pulse rate, current drive level to the motor (0, 19, 60, and 100% of maximum), and the number of steps to move between the open and closed positions. During normal operations, the motor is driven at 120 steps per second with 60% of the maximum possible drive current to the motor, which provides sufficient torque and inertia margin to open or close the light blocker. For emergency and test situations, the IC can override TPG control of the light blocker operation by writing to a TPG register. In those situations, the IC can send direct commands to move the light blocker a desired number of steps in a given direction.

3.1.3.3. Visible Stimulator. Although not a mechanism, the visible stimulator is described in this section, since it is packaged in the light blocker. The visible stimulator is used as an on-board diagnostic for the CCD systems. A light emitting diode (LED) is mounted inside the light blocker mask, aimed at approximately the center of the light blocker blade in front of the CCD. The LED is powered by one of the instrument heater circuits, supplied by the flight system thermal control subsystem. The LED intensity is a function of both the LED temperature and the current supplied to the LED. None of the voltages on the heater circuits that supply the LEDs is regulated, and the light blocker temperature may vary during the mission, so the stimulator is not an absolute intensity measurement. Instead, it is meant to be a method of checking for high spatial frequency changes in the CCD sensitivity – i.e. dust or other obscurations on the CCD itself – and checking for gross changes of gain or offset across quadrant boundaries.

3.2. THERMAL

The thermal design of the instruments is highly integrated with the spacecraft thermal and mechanical design. The instruments sit on the opposite side of the large (7 m^2) solar panels and so have excellent views of cold space for almost all of the mission, including the encounter with comet Tempel 1.

The IR spectrometer is the major driver in the instrument thermal design. With a cutoff wavelength of 4.8 μm, the IR detector will be saturated in its normal readout time (3 s) if it looks at a room temperature background. Further, the IR detector dark current will also saturate the detector full-well in a readout time, if the detector temperature is > 110 K. The thermal design made use of the clear view of cold space to cool the detector and the SIM bench passively. The SIM is cooled by its exposed upper surface, which has been extended about 8 cm beyond the SIM structure to increase the cooling efficiency. The detector is cooled by a two-stage passive radiator mounted to the SIM optical bench. The second (warmer) stage is isolated from the SIM bench by three fiberglass composite flexures. The primary radiator is isolated

from the second stage by similar fiberglass composite flexures. The flexures are thin to reduce thermal conductivity, but are stiff enough to maintain the detector spacing and survive the mechanical loads at launch. The effective surface emissivity of the radiator surfaces is enhanced by adding aluminum honeycomb in surface pockets. Thermal-vacuum tests along with correlated thermal models predict that the bench will operate at ≈ 136 K, and the IR detector will operate at <85 K at the encounter, which will produce $<1,000$ DN/s of dark signal.

The CCDs benefit from cold operation, since their dark current is also reduced. The HRI CCD, which is mounted to the SIM bench, is actually warmed to 160 K by integrated heaters. This reduces the risk of mechanical stress to the detector, which has been tested as low as 155 K. The MRI CCD is mounted directly to the MRI telescope structure. Most of the MRI telescope is covered with multi-layer insulation, but part of the top surface of the telescope cover is left uncovered to aid in cooling of the structure and CCD to around $-85\,^{\circ}$C. The ITS structure is largely internal to the impactor spacecraft, so it cannot cool the CCD effectively. Therefore, a dedicated radiator and copper heat pipe were added with a direct link to the ITS CCD. The radiator looks out the front of the impactor spacecraft so that it will cool the CCD during the cruise, as well as the 24 h of the impactor spacecraft free flight before impact. During this period, the ITS CCD will be maintained at less than $-30\,^{\circ}$C.

All of the critical optical components are fitted with heaters so that during the first few days after the launch their temperatures can be maintained above those of the rest of the structure. These heaters are intended to reduce the risk of contamination in the critical time period after launch.

Ground tests determined that the focus of the telescopes was within specifications when the water content of their graphite epoxy structure was reduced below 10% of saturation. In ambient conditions in the launch vehicle fairing, the composite structure will absorb moisture. Therefore, to reproduce the proper focus, the water in the structure must be reduced to less than 10% of saturation in flight. A set of heaters was added to the structure of each telescope so that it could be raised to temperatures above $0\,^{\circ}$C to bake out the moisture. The heaters are expected to raise the temperature to about $5\,^{\circ}$C, and the HRI telescope structure will require 30–40 days to reach 10% of saturated moisture content or less.

Since instrument thermal control must be maintained even during periods when the instruments are not powered on, all of the heaters are controlled by the spacecraft thermal subsystem. The spacecraft thermal subsystem also maintains a set of thermal monitors for the key components. Each instrument electronics subsystem has 10 platinum resistor thermal monitors distributed among the structure and optics on that instrument, as well as five integrated circuit temperature transducers (Analog Devices AD590) to monitor the instrument electronics board temperature (there are six on HRI). These temperature sensors only supply telemetry to the spacecraft and ground when the instrument electronics are powered on and analog data collection is commanded on.

3.3. DETECTORS

There are two types of detectors on the Deep Impact instruments. A CCD detector, with response from 0.3 to 1.1 μm, is used on all three instruments. An infrared focal plane array (IR FPA) with response from less than 1.0 to a 4.8 μm cutoff is used on the HRI IR spectrometer only.

3.3.1. *CCD*

The CCDs are Fairchild Imaging (formerly Lockheed Martin Fairchild) custom design split frame transfer CCDs (ID CCD424) with four independent quadrants, each with an associated output amplifier. The image area has 1,024 × 1,024 pixels, while both storage regions have 1,024 × 530 pixels. The storage areas are over-sized to allow for image mask mis-alignments. The pixels are 21 μm^2, producing an image area that is 2.15 cm on a side. Figure 9 shows the CCD architecture.

Image transfer and readout are controlled by three clocking phases in both the parallel and serial directions. Each quadrant is fully independent in the parallel direction (in fact, the image and storage regions have independent gates), while one phase is shared on either end in the serial direction. Charge can be transferred across the center line of the CCD in the parallel direction. This means that any pixel may be read out of any of the four amplifiers on the CCD – although this option is not implemented on DI.

With the large pixels, detector full-well is measured at about 400,000 electrons. This high capacity was implemented in response to an early requirement to be able to image the comet and guide stars simultaneously within the dynamic range of the CCD system. While subsequent navigation design has moved away from this requirement, the large full-well does help guard against saturation due to uncertainties in the surface brightness of the nucleus and coma. The image area is thinned to about 17 μm thickness and the image is formed on the back of the CCD which increases quantum efficiency, especially in the near-UV and blue. The quantum efficiency of most of the CCDs characterized for DI peaks at a value of 0.7 at a wavelength of about 600 nm as seen in Figure 10. The data in the figure were extrapolated above 900 nm, since the CCD characterization equipment was limited in wavelength coverage to 900 nm. The CCDs were tested at the flight readout rate of 187,500 pixels/s. The CCD test set was not designed to separate the test set noise from the CCD noise, but the read noise of the combined test set system was 10–12 electrons. This is a small contribution (noise combines in quadrature) to the flight system read noise which is slightly less than 28 electrons (about 1 DN).

3.3.2. *IR FPA*

The IR detector used for the DI IR spectrometer is a hybrid array with a mercury cadmium telluride (HgCdTe) infrared sensor indium bump-bonded to a Rockwell Science Center HAWAII-1R multiplexer. The readout circuit was originally developed for the HST Wide-Field Planetary Camera III instrument. For Deep Impact,
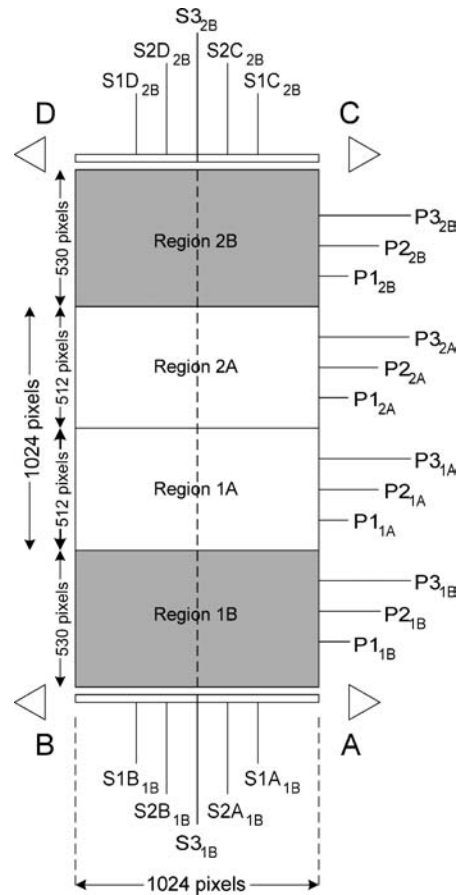
Figure 9. Deep Impact CCD architecture. Regions 1A and 2A are the imaging area. Regions 1B and 2B are the storage regions.
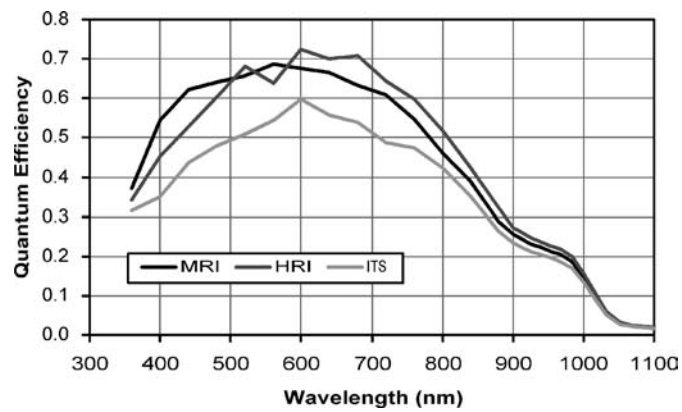

Figure 10. CCD quantum efficiency. The quantum efficiency for all three flight detectors is shown as measured in the CCD characterization test set.
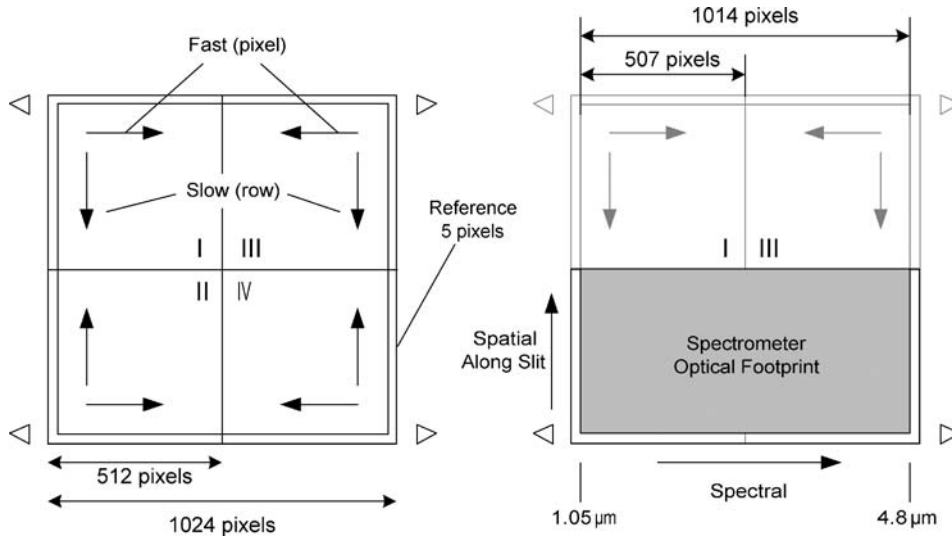
Figure 11. IR FPA architecture. The figure on the left shows the architecture of the full HAWAII-1R array. The figure on the left shows how the spectrometer is mapped to one half of the array.

a custom MWIR HgCdTe substrate with a cutoff wavelength at 4.8 μm was developed. The CMOS readout array has 1,024 $\times$ 1,024 pixels that are 18 μm^2, and has four electrically independent quadrants with separate readout amplifiers. The optical system was designed such that only two of the quadrants are illuminated. (Thus, while each IR image only has two halves, these halves are still called quadrants.) The detector orientation was chosen such that the fast readout direction is along the spectral direction, while the slow readout is along the slit, in the spatial direction, as seen in Figure 11. Therefore, the spectrum of each spatial sample has the same time history. Because the detector is read in a ripple mode, one spatial sample will have a slightly different time history than the another. Section 4.1.2 describes the timing from line to line.

The detector has five reference rows on each edge. Four of the rows have a fixed capacitance, while the fifth (outer) row has a series of four capacitance values, cycling across the detector. The detector QE is shown in Figure 12. The cutoff wavelength is 4.8 μm. The QE drops rapidly below 2 μm due to a passivation layer added to the HgCdTe surface. This layer reduces significantly the detector readout noise, which somewhat compensates for the low sensitivity at short wavelengths. Further, surface spectra are expected to look much like solar spectra, so that the greatest fluxes will be at short wavelengths. As seen in Section 5.3.5, the low QE at the short ends flattens out the response for surface spectra.

In the DI flight operating configuration the detector full-well is measured at 120,000 electrons. With the 4.8-μm cutoff, the detector dark current exceeds the full-well for the minimum 2.9-s full-frame readout time, unless the detector
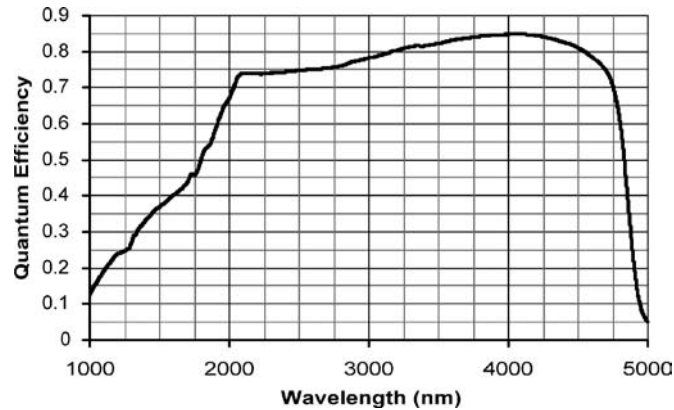
Figure 12. IR FPA quantum efficiency. The steep change below 2 μm is due to a passivation layer on the HgCdTe detector layer to reduce detector readout noise.

temperature is less than 110 K. The radiative cooler described in Section 3.2 is expected to cool the detector to 85 K or less. At this temperature, the detector dark current produces about 3,000 electrons in a nominal readout time, less than 3% of the detector full-well.

To achieve this temperature for the IRFPA, the number of linkages between the detector and the radiator was reduced as much as possible, while still protecting the mechanical integrity of the FPA. The cooler, made of aluminum, has a much greater coefficient of thermal expansion than the detector. The detector is bonded directly to a molybdenum substrate , which is mounted to a flexured BeCu support, which is mounted directly to the aluminum cooler. This stepping of materials with gradual changes in expansion coefficient results in a low mechanical stress on the detector substrate, which protects the relatively delicate indium bump bonds. The detector has survived six thermal cycles from room temperature to operating temperature with no detectable increase in non-operable pixels. Only the thermal cycle in space remains at the time of writing.

A mask is mounted immediately in front of the IR FPA to shield additional responsive areas of the array from out-of-spectrum light.

3.4. ELECTRONICS AND SOFTWARE

Each instrument has two electronics boxes associated with it: a main electronics box, mounted internal to the spacecraft, and a CCD pre-amp/clock driver box. Figure 13 shows the placement of the main HRI and MRI electronics boxes relative to their respective instruments. Because the boxes are mounted internally, they require less energy from the spacecraft to maintain the desired operating temperature. With these boxes mounted on the spacecraft, as shown in the figure, the cable lengths between the electronics and main instrument structure are 1 m or less.
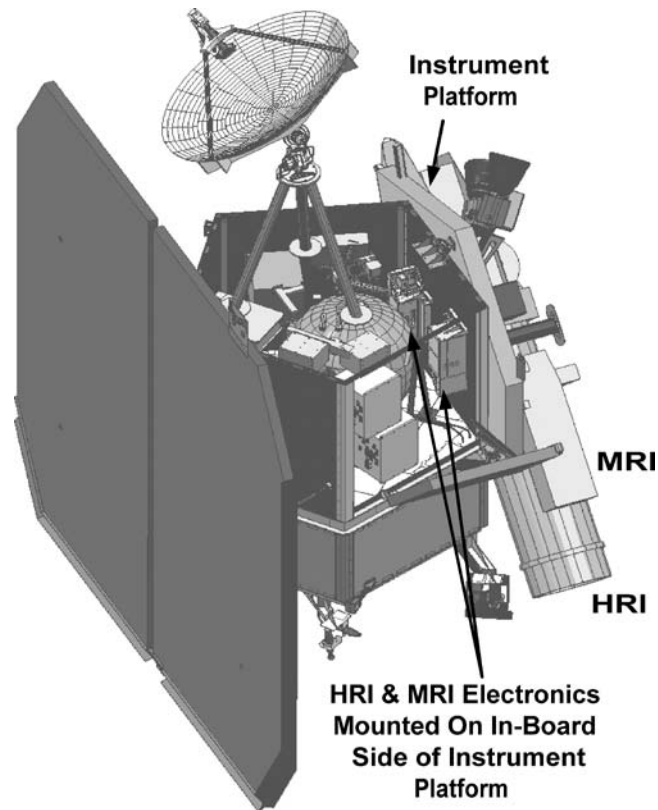
Figure 13. Instrument electronics box placement in Deep Impact spacecraft. The HRI and MRI main electronics boxes are mounted internal to the spacecraft structure. They are mounted on the panel adjacent to the instruments to reduce the cable length to less than 1 m.

3.4.1. *Instrument Electronics*

An early decision in the development of the DI instrument electronics was to have a modular electronics design, with one main function for each board, and one main electronics box for each instrument. Not only did this allow for parallel development, test and final production of each board and box, it also allowed for packaging that reduced the electrical noise on the sensitive detector readout boards. The main electronics box contains a motherboard, which provides interconnects between the specific subsystem boards. There are four daughter boards in the MRI and ITS boxes and the five daughter boards in the HRI electronics box. Physically, the boards conform to a 120 mm tall 6U VME form factor. Electrically, the connector pinouts are not VME standard, but are custom to DI. The boards are shown in the block diagrams (Figures 1 and 2), and their main functions are described in Table III. There is no image storage or manipulation in the instrument electronics. In fact, other than adding an image header, the IC acts only as a data conduit to the spacecraft

TABLE III

Boards in the main instrument electronics boxes.

Board	Functions
Instrument controller (IC)	Command and Control
	Telemetry collection and broadcast to SCU
	Error handling and notification
	Image data flow from other boards to SCU
Low-voltage power supply (LVPS)	Power conditioning from S/C bus
	Power distribution to other boards
Mechanism and telemetry (MTLM)	Mechanism control and monitoring
	Analog telemetry collection
Visible system (CCD)	CCD exposure command execution
	CCD timing pattern generator
	CCD analog data conditioning and digitization
Infrared system (IR)[a]	IR exposure command execution
	IR analog data conditioning and digitization
	IR FPA bias generation and adjustment
	IR FPA timing pattern generator
	IR FPA clock driver

[a]HRI only.

control units (SCUs) for the science images from the detectors. The IR and CCD boards are shielded from the other boards by placing aluminum spacers between those boards and adjacent boards. This reduces electrical cross-talk between the detector boards, and the IC board that handles high-frequency data transmission, and results in detector systems that meet their noise performance requirements. The following sections describe the functionality and design of each board in more detail. With the exception of the IR board, which is only in the HRI electronics box, the electronics box for each instrument contains one of each of these boards.

3.4.1.1. Low-Voltage Power Supply. The LVPS receives unregulated spacecraft bus power and supplies regulated voltages to all other boards in the electronics box. The LVPS will operate as required for an input bus voltage between 24 and 35 V, which are the required limits on the spacecraft bus. To reduce detector system cross-talk, the LVPS supplies each board with its own set of isolated regulated voltages, even those boards that use common voltages (e.g. 5 V). The LVPS switching frequencies are derived from the operating pixel frequencies of the CCD and IR detector signal processing boards. This ensures that LVPS switching noise is synchronized with the detector clocking, making sure switching does not happen when the detector board is performing a critical measurement.

The LVPS board also supplies the system reset to the entire electronics system, to ensure that the electronics are in the reset condition during either power-up or power-down transition.

3.4.1.2. Mechanism and Telemetry (MTLM) Board. The MTLM board contains the pulse drivers for stepper motors that drive the two mechanisms on each instrument – the light blocker and the filter wheel (ITS has no filter wheel). These drivers can run at 0% (off), 19, 60 and 100% of their current capacity and at an arbitrary step rate. Both the current level and step rate can be set by external command. On instrument power on, the current level is set to 60%, and the rate to 120 steps/s, which supplies sufficient torque to the motors. Commanding the drivers to 100% current capacity and reducing the step rate will result in greater torque on each motor. This can be used as a contingency to overcome any unforeseen mechanism "stiction" that may develop during the mission.

The MTLM board is also the focal point of all analog telemetry collected for that instrument. The MTLM FPGA cycles through its set of analog telemetry points every 2 s, and transmits the data to the IC on the same schedule. This analog telemetry is stored in software registers and is sent out as instrument telemetry when requested by the spacecraft. Some of the analog telemetry is placed in the 100-byte image header when the image is transferred to the SCU.

3.4.1.3. Instrument Controller Board. Figure 14 shows a block diagram of the IC board. The design is centered around a radiation-tolerant TSC695F single-chip SPARC 32-bit microprocessor. The processor hosts a real-time operating system that receives commands from the spacecraft *via* the 1553 bus. The IC communicates with the other boards *via* 3-Mbit/s low-voltage differential signaling (LVDS) lines that are controlled by the IC FPGA. Data from the detectors are routed through the IC FPGA and to the SCU by means of a 12-Mbit/s LVDS interface.

The instrument flight software image is stored redundantly in 2 MB of non-volatile EEPROM. On instrument power-up, the EEPROM image is transferred to 4 MB of SRAM, and the processor operates from the software image in SRAM. The choice of which EEPROM image to transfer is controlled by a bi-level relay, which is toggled by the remote interface unit on the spacecraft. To accommodate quick turn-on during the encounter, another bi-level relay controls whether the boot process includes a memory check or not. Normal bootup (including the memory check) takes 28 s, while the fast bootup takes 21 s, a 7-s savings.

The IC is also responsible for generating a 100-byte image header placed in each image that is transferred from the instrument electronics to the spacecraft control unit. The header contains routing information from the exposure command, software and hardware states from the flight software, analog telemetry and a time stamp based on the spacecraft vehicle time code (VTC). The timing of the header generation is important because that determines the time that is associated with
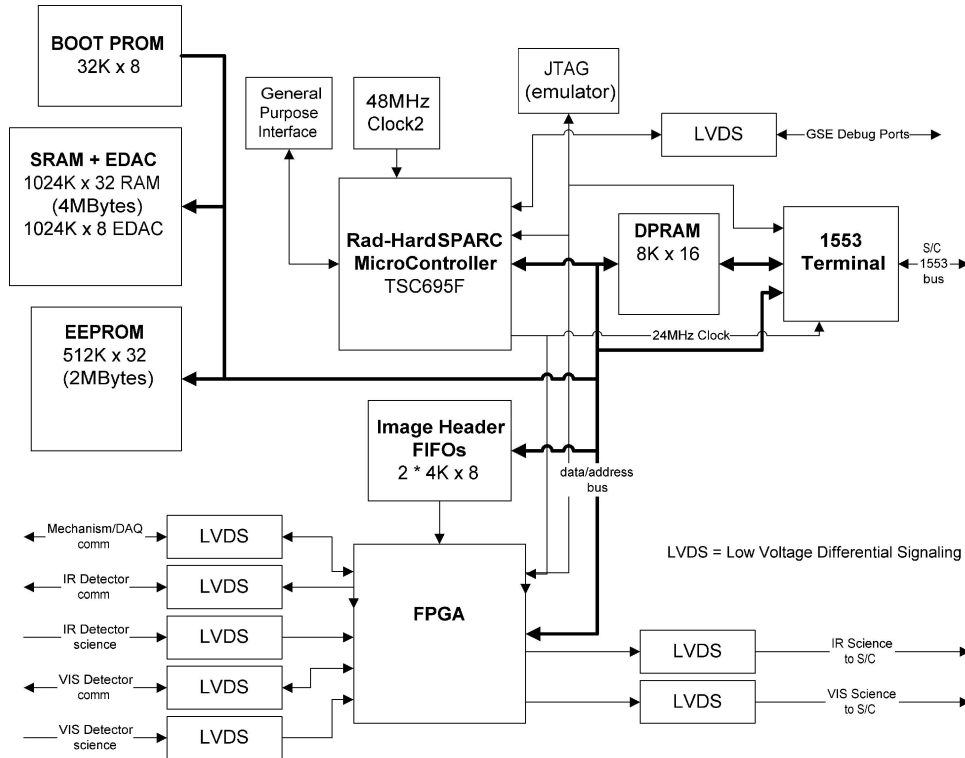
Figure 14. Instrument controller board block diagram.

that exposure. The detailed relationship between the header time stamp and the exposure time of the images is discussed in Sections 4.1.1 and 4.1.2.

The VTC is collected from the spacecraft *via* the 1553 command channel. The sequence is basically "at the tone the time will be. . .", followed by a tone. The spacecraft sends out a message that includes an upcoming VTC. The IC stores that VTC in a register. The spacecraft then sends a message that tells the instrument to set its internal time to the VTC that was just transmitted. The accuracy of the message and the latching maintain the spacecraft to instrument VTC to within 64 μs. The VTC is updated at a 1 Hz rate.

3.4.1.4. IR Signal Processing Board. The IR board FPGA contains the TPG that drives the readout of the IR FPA. Since the FPA is a digital multiplexer that is operated by TTL signal levels, and because the FPA output amplifiers are capable of driving a differential signal over a cable 1 m in length, there was no need for an IR FPA pre-amp close to the detector. Thus, the detector biases are also set on the IR signal processing board. Since the performance of the IR FPA is sensitive to these biases, three of them are controlled by means of 8-bit DACs that are controlled

by external commands. The output of the IR FPA produces a zero signal level at a positive voltage (around +5 V). Two similar 8-bit DACs, one for each quadrant, are used to adjust these offsets to be on-scale for the 14-bit A/D converter. The 14-bit A/D converter and 120,000-electron full-well led to selecting a conversion gain of 15 electrons per DN.

The IR FPA is fundamentally different from the CCD in that it essentially has a portion of an amplifier in each pixel. In many applications this is desired, since it allows multiple non-destructive readouts of the array. The best noise performance for detectors of this type comes from doing correlated double sampling, i.e. each integrated signal is correlated with the offset value from the beginning of that integration. To accomplish this, an offset value must be read from each pixel before the charge is collected in that pixel during the integration period. For many IR systems this is done by collection of both a reset frame (the offset levels) and a read frame (the integrated levels) with a subsequent subtraction during image analysis; however, this results in two images per measurement. We reduce the number of images required to be returned by incorporating memory on the IR signal processing board in which the reset frame is stored. The subtraction that results in a correlated image is then calculated on the IR board during the readout of the integrated frame. The memory and storage of the offset frame also allows for 2×2 binning of the images on the IR signal processing board.

The details of the readout modes for the IR detector are discussed in Section 4.1.2.

3.4.1.5. CCD Signal Processing Board. The FPGA on the CCD board contains the TPG that drives the readout of the CCD. The clocking lines from the FPGA go to the clock driver board, which is part of the CCD pre-amp clock and bias box (see the following section) where the timing patterns are amplified to their voltage rail values. The CCD board also receives differential signals from each quadrant of the CCD, after they have been conditioned by the CCD pre-amp. The CCD board performs a clamp and sample operation during each pixel readout, based on TPG signals, producing a correlated double-sampled analog signal. The board then converts the analog signal into a 14-bit digital number (DN) by a 14-bit A/D converter. The digital signal is transferred first to the IC and finally to the SCU. With the 14-bit resolution and the requirement to span the data over the originally expected 450,000-electron full-well of the CCD, the conversion gain of the CCD system was selected to be 30 electrons per DN.

The details of the readout modes for the CCD system are described in Section 4.1.1.

3.4.1.6. CCD Pre-Amp, Clock and Bias Box. The separate CCD pre-amp, clock and bias box (pre-amp box for short) contains two printed circuit boards. One board has four 1:1 amplifier circuits that convert the CCD output video signal from single ended to differential signal, allowing for low noise transmission over a 1 m cable

length. The DC bias voltages required by the CCD are also set on this board. The other board contains a set of voltage converters that set the upper and lower rails of the clock lines that transfer the charge on the CCD. These convert a TTL signal from the TPG on the CCD signal processing board into the clocks that drive the CCD charge transfer. The two boards are separated by a solid metal partition so that the amplifier does not pick up noise from the clocks. The pre-amp boxes are located within 18 in. of the CCDs on each instrument. This means that for the flyby spacecraft they reside on the instrument platform, and therefore have heaters and temperature sensors to maintain them above their allowable flight temperatures and maintain a stable operating temperature at encounter. For the ITS, the pre-amp boxes reside within the cover of the impactor spacecraft and will not be at risk of cooling below acceptable operating temperatures.

3.4.2. *Software*

The software for the DI instruments leveraged heavily off the Spitzer (formerly SIRTF) IRS and MIPS instrument software development. Figure 15 shows the major components of the instrument flight software. All code is written in ANSI-C.

The DI instrument software performs the following main functions:
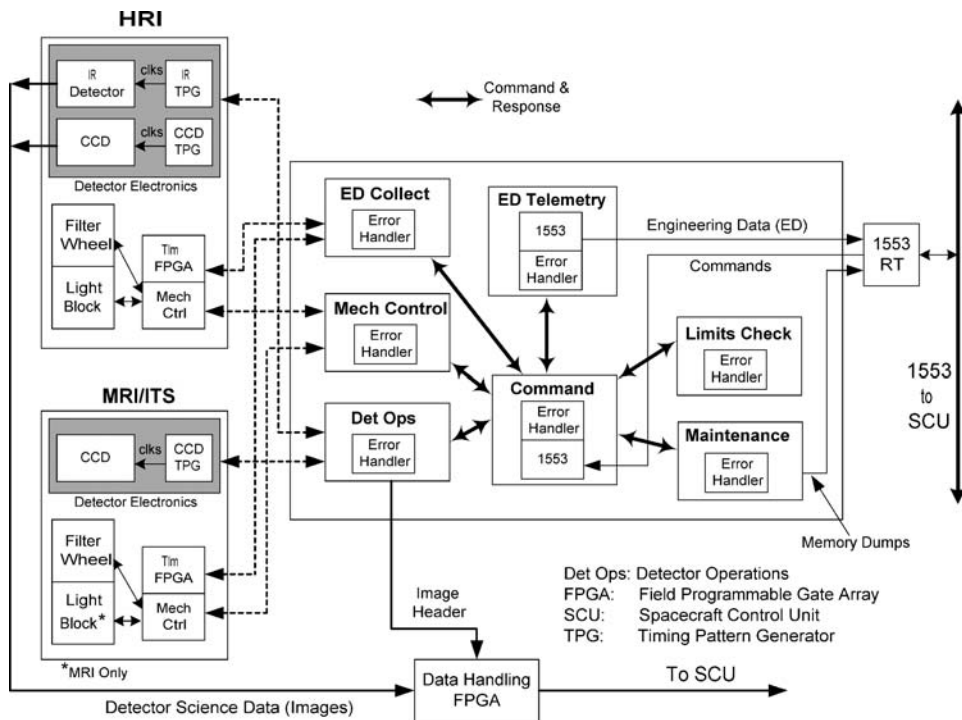
1) Receive and process command data.

Figure 15. Instrument flight software architecture diagram.

2) Control and coordinate the HRI/MRI/ITS instrument activities based on defined operational parameters within the accepted commands.
3) Configure the visible detectors and infrared detector, and control the collection of the science image data *via* the detector electronics interface.
4) Configure the instrument mechanisms (filter wheel, light blocker) for mechanism calibrations and for observations *via* the mechanism electronics interface.
5) Gather, format and output engineering telemetry data.
6) Initiate science data-taking and the flow of science data images to the spacecraft computer (SCU) *via* the science data channel.
7) Monitor instrument safety parameters and maintain the instrument in a safe configuration.
8) Perform memory self tests.
9) Initialize and maintain the Instrument Payload electronics and software systems of the instrument.
10) Gather calibration data. For mechanism calibration, the calibration data are a subset of the engineering data routinely collected by the Instrument Payload Flight Software and forwarded to the SCU.

3.4.2.1. Boot State. When power is applied to the main electronics of any instrument, or when a reset occurs, the IC processor will begin execution of the boot state software stored in a radiation-hardened PROM non-volatile memory area. The primary purpose of the boot state software is to perform basic memory testing, followed automatically by the copying of one of two software images from EEPROM to RAM, followed automatically by the transfer of control to that software image in RAM. Since the boot-code will exist in PROM, it will not be possible to modify the boot-code after launch.

3.4.2.2. Operate State. Once the instrument has completed the steps described in the boot state, it transitions to the operate state. In this state, it will perform on demand the following activities:

1. Accept and execute commands received over the 1553 interface.
2. Collect and monitor engineering data.
3. Configure and control the mechanisms.
4. Configure the detectors.
5. Initiate science data-taking and the flow of science images to the SCU.
6. Format and output engineering telemetry data to the 1553 interface.
7. Provide the ability transfer data between instrument memory and the ground system *via* the spacecraft SCUs.

In addition to these functionalities, the software also performs some rudimentary fault protection, as well as interfacing to the spacecraft fault protection system. This includes error reporting from software and hardware monitors. There are 498 errors that can be reported. The software also monitors high and low limits on analog

telemetry points – voltages and temperatures – reporting out of limits conditions as an error. The limits reside in an internal software table that includes a persistence count for each telemetry point – e.g. temperatures must be out of limits for 30 consecutive queries before an error is posted.

If an error is deemed sufficiently bad, the instrument will post a request for action to the spacecraft fault protection system. The possible actions are to reset the IC, power cycle the instrument, or turn off the instrument and alert the ground. The severity of the action can also be determined by the criticality of the current spacecraft state. Errors that would result in a request for power-off during the 6-month cruise may result in simply posting the error when the spacecraft is engaged in the encounter with Tempel 1.

4. Data Format and Pipeline

This section describes the different imaging modes, including details on the timing, and the data pipeline. The TPGs on the IR and CCD electronics boards are able to produce several different imaging modes each to accommodate requirements on the imaging sequence. As such, not only do the instrument electronics designs need to be dynamic in accepting imaging command parameters to produce these modes, the rest of the data pipeline, all the way to the spacecraft control unit non-volatile memory, must react correctly to the different imaging modes.

4.1. IMAGING MODES

4.1.1. *Visible (CCD) Imaging Modes*
One mission requirement is to observe the impact at imaging rates significantly greater than 1 Hz, which can only be accomplished with image sub-framing. Further, at times when the nucleus is not resolved, or does not fill up the field of view of the instrument, a sub-frame image will produce the same information on the comet nucleus surface while taking up much less of the limited storage space on the spacecraft computer. With four output amplifiers, symmetric sub-framing of the CCD results in approximately a factor of two reduction in readout time for each factor of two reduction in linear image size. Thus, the 1.4-s readout of the full $1,024 \times 1,024$ pixels is reduced to about 0.7 s for reading out 512×512 pixels. The CCD imaging modes are shown in Table IV. All the sub-frame modes are symmetric about the center of the CCD, i.e. each quadrant makes up one-quarter of the stored image.

A second consideration for the imaging modes is whether the light blocker is used for each image. The light blocker can be controlled by either a direct command to the mechanism FPGA, or by the CCD TPG. The light blocker was added so that during the readout of a full-frame image, the scene in the imaging area does not saturate

TABLE IV

Visible (CCD) imaging modes.

#	Mode	Stored size (X and Y)	Serial O'clocked size (X)	Serial O'clocked co-add	Parallel O'clocked size (Y)	Parallel O'clocked co-add	Light blocker used on each image	Dither?
1	FF	1,024	8	0	8	4	Yes	No
2	SF1	512	4	0	4	4	Yes	No
3	SF2S	256	4	0	4	4	Yes	No
4	SF2N	256	4	0	4	4	No	No
5	SF3S	128	2	0	2	4	Yes	No
6	SF3N	128	2	0	2	4	No	No
7	SF4O	64	0	0	1	2	No	No
8	SF4NO	64	0	0	0	0	No	No
9	FFD	1,024	8	0	8	4	Yes	Yes

TABLE V

Visible mode frame-to-frame times.

#	Mode	Minimum commanded t_{INT} (ms)	F-T-F time for minimum t_{INT} (s)	F-T-F time for $t_{INT} = 100$ ms (s)
1	FF	0	1.634	1.735
2	SF1	0	0.737	0.838
3	SF2S	0	0.430	0.531
4	SF2NS	4	0.232	0.328
5	SF3S	0	0.312	0.413
6	SF3NS	4	0.113	0.209
7	SF4O	4	0.062	0.158
8	SF4NO	4	0.062	0.158
9	FFD	0	1.634	1.735

the CCD and bleed charge into the storage area, corrupting the image currently being processed. For the smallest sub-frames, the readout times are significantly shorter and the light blocker should not be required to prevent charge bleeding. For modes 1 and 2, the light blocker is used for each image, whereas for modes 7 and 8 (64 × 64 pixel sub-frame size) the readout time is 0.06 s as shown in Table V, and the light blocker is not required. For intermediate image sizes (128 and 256 pixels square), there is a choice of whether the light blocker is used or not. For modes where the light blocker is not used, the ratio of exposure time to frame-to-frame time becomes very efficient, with only a 10- to 15-ms delay between the end of a previous exposure and the start of the next.
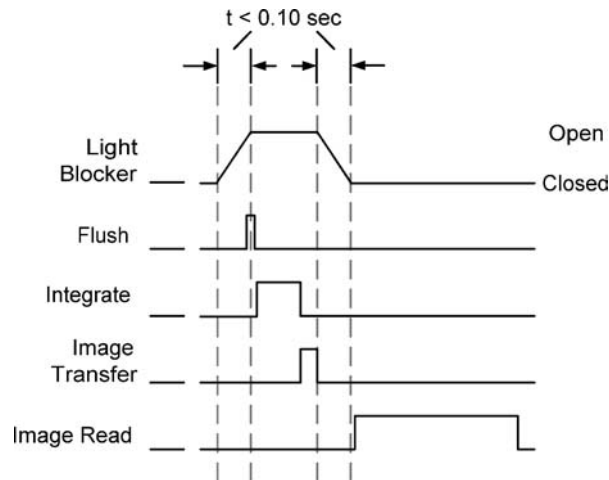
Figure 16. CCD image exposure sequence for modes where the light blocker is used for each image. The timing is not to scale. Generally, a trace shows inactive low, active high – e.g. image transfer is active just before the light blocker starts to close. Note that the image is not read out, while the light blocker is moving to avoid electrical noise from the stepper motor contaminating the image data.

The imaging cycle when the light blocker is used for every image is shown in Figure 16. The overall frame time is increased by the opening and closing of the light blocker. We chose not to set the timing so that the CCD electronics are reading the CCD while the shutter is moving to avoid inducing noise in the CCD data. Upon receiving the exposure command, the CCD TPG begins by opening the light blocker. This takes slightly less than 100 ms. At about 50 ms into the light blocker motion, the TPG begins flushing the CCD. This is the same pattern as transferring the charge from the image area to the storage area, but in this case the pattern continues until the image and storage area have been completely transferred five times. The end of this flush happens after the light blocker is completely open, and designates the beginning of the integration period. The TPG waits for the commanded integration delay time and then begins the frame transfer. The transfer takes 5.7 ms. Once the transfer is complete, the TPG closes the light blocker. This also takes the same time as the opening process, 100 ms. When the light blocker is closed, the TPG either begins the readout of the CCD for the full-frame modes (1 and 9) or performs a partial transfer of the storage area to get to the first row saved for a sub-frame image. When the last row of pixels is read out, the TPG FPGA either begins the entire cycle again if the command requested more than one image, or on the final image it closes out its registers, sends a message back to instrument flight software, and is ready to receive the next exposure command.

For modes that do not use the light blocker between images, the cycle is shown in Figure 17. As in the light blocker mode, the first action that the TPG takes is to open the light blocker. It also performs the similar five-image flushes starting
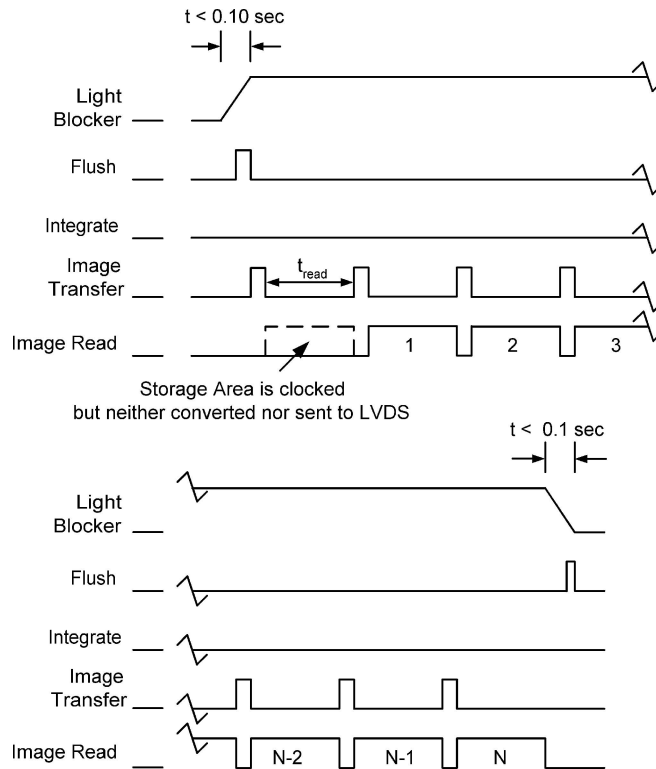
Figure 17. CCD multi-image exposure sequence for modes where the light blocker is not used for each image. In this case, *N* images were requested in the image command. The format is the same as Figure 16. The timing is not to scale.

50 ms into the light blocker move. In this case, however, the TPG begins the cycle by immediately starting a frame transfer at the end of the flush. The image that was transferred was not integrated for the proper time (it does not include the readout time from a previous frame), so while the TPG does read the image out of the CCD to set the proper timing, it does not command conversion of the charge into digital signals and therefore does not transfer an image to the SCU. As soon as the TPG finishes the readout, and waits for the commanded integration time, it begins another frame transfer and immediately begins the readout of the CCD. This image, the first of the sequence, is converted to digital signals and transmitted to the SCU. This cycle is repeated for the number of images commanded (1–255). After the last image is read out, the TPG then closes the light blocker, clears the FPGA registers and signals the software that it is ready to receive the next image command. Note that in this mode, the true integration time is actually the minimum frame-to-frame time minus the frame transfer time plus the commanded integration time.

An important parameter to understand for interpretation of the data for both science and the navigation, is the relationship of the time stamp in the image

TABLE VI

IR imaging modes.

#	Mode mnemonic	Mode	Stored image size	Minimum exposure time (s)	Frame-to-frame time for minimum exposure (s)
1	BINFF	Binned full frame	512×256	2.86	2.862
2	BINSF1	Binned sub-frame 1	512×128	1.43	1.432
3	BINSF2	Binned sub-frame 2	512×64	0.71	0.717
4	UBFF	Unbinned full frame	$1,024 \times 512$	2.86	2.862
5	ALTFF	Alternating binned full frame	512×256	1.43	2.868
6	DIAG	Diagnostic	$1,024 \times 512$	1.43	1.432
7	MEMCK	Memory check	$1,024 \times 512$	N/A	2.862

header to the center of the integration for that image. For the CCD the timing is straightforward: the time stamp is latched into the header when the TPG sends the signal to transfer the charge from the image area to the storage area. This means that whether or not the image mode uses the light blocker for each image or not, the center of integration is the time stamp minus half the true clock-stopped integration time for that image.

4.1.2. *IR Imaging Modes*

The IR imaging modes are shown in Table VI.

The IR detector modes are divided into two different readout methods; interleaved readout and alternating readout.

The Hawaii 1-R allows an entire row to be reset at one time and permits a very efficient interleaved readout method. A row of integrated values is read out (on the first pass, though these values are discarded). That same row is then reset, and the offset values are read from that row, and immediately stored in memory in preparation for the next exposure. The TPG continues this process through each row of the detector. When it reaches the end of the detector it returns to the beginning and reads out the integrated values from the first row, subtracting off the corresponding offset value stored in the IR board memory on the previous cycle. With this interleaved readout method, the only integration time lost is the time to reset and read a single row, provided that multiple exposures are taken one after another by a single command.

In the alternating readout method, a row of the detector is reset and the offset values are read into memory. The TPG continues with only this operation until it reaches the end of the detector. The TPG then returns to the beginning of the detector and reads through each row, reading the integrated values and subtracting their corresponding offset values. The frame-to-frame time for alternating readout is the same (for a similar sized frame) as for the interleaved readout, but only half of

the time is dedicated to integrating signal in the pixels. This method is useful if the approximately 3 s for integration in the interleaved readout will result in saturation. But from a time series standpoint, half of the sampling time is missing. Thus, a fast event that happens during the offset readout of the alternating mode will be missed. The interleaved sampling will not resolve the same fast event, but it will capture the average signal during the event, while the alternating readout has a 50% chance of missing it entirely. Modes 1–4 use the interleaved readout method, while modes 5–7 use the alternating readout method.

As with any multiplexer readout, each row of the DI IR detector has slightly different start and stop times for integration, while the total integration time for each row is the same. This can be problematic when trying to interpret a dynamic scene (as is expected at the time of impact), but the timing for the DI detector readout is systematic and repeatable, and is well correlated to the time stamp that accompanies each image.

Modes 1–3, and 5 make use of the ability of the IR signal processing board to bin the output 2×2. Modes 4 and 6 leave the pixel data unbinned rather than using the 2×2 binning option. In mode 6, the offset image and the integrated image are not subtracted in the instrument, but are transferred to the spacecraft individually. This mode allows a check to verify that both images are within the range of the A/D converter. Mode 7 allows a check of the memory on the IR signal processing board that is used for correlated double sampling and binning. The FPGA loads either a single value or a double ramp pattern into memory and then reads the memory out into the image data stream. This test is intended only to check the integrity of the memory and does not test the analog portion of the IR electronics.

As mentioned in Section 3.3.2, the IR detector is read out in a ripple mode, and each spectral line has a slightly different time history. The frame-to-frame time for a full-frame interleaved image is 2.862 s. This is the time, ignoring any overhead, taken to read 512 physical rows of the detector. Using this as a quick measurement shows that each row is read in about 5.5 ms for interleaved modes. This is actually the time taken to read through the row twice, once for the integrated values and once for the reset values. For mode 4 (unbinned, interleaved), this is the amount of time between the beginning of integration for one row and the beginning for the next row. Two rows that are 20 rows apart would have integrations that begin approximately 110 ms apart.

For binned interleaved rows, the row-to-row time is doubled, since it takes four reads of each row to produce a single binned row. Thus, for modes 1–3, the integration time offsets are approximately 11 ms times the difference in row number apart. For the alternating readout modes, the integration time offset for binned and unbinned modes are a factor of 2 shorter, approximately 2.75 ms per row for unbinned, and 5.5 ms per row for binned.

This shows the timing between rows, but an important parameter is to know how this relates to the instrument time code (ITC), which is synchronized to the VTC at a 1 Hz rate, that is placed in an IR image header. Like the CCD time stamp, the IR

TABLE VII

Parameters to determine line time relative
to the image header time stamp.

IR mode	A (ms)	B	C (ms)
1	11.01	1	0
2	11.01	1	0.341
3	11.01	1	1.02
4	5.50	0	0
5	11.01	1	0
6	2.75	0	0

time stamp is latched into the header buffer on the IC by timing signals from the IR TPG. The IR TPG sends a signal to the IC 200 μs before it is ready to begin reading a new set of integrated values. The IC then loads exposure command parameters and telemetry into the header FIFO buffer and sends that header over the LVDS interface to the spacecraft control unit (SCU). When the IR TPG begins the new readout of the detector it sends a second signal to the IC, which then latches in the current ITC from its register, into the header buffer and sends it immediately to the SCU. It can do this in 4–5 μs, but the latching of the time is accurate to within two 12-MHz clock cycles, or ±166 ns. The limiting knowledge of the image time to the spacecraft time is the 64 μs synchronization of the 1553 discussed in Section 3.4.1.

Now the IR TPG begins the sampling of the detector. Even in unbinned modes (4 and 6) the TPG will take two of its clock cycles, 5.33 μs each, in housekeeping and overhead before it will sample the first pixel. For the binned modes, it will take one full row of readout and calculation before it starts producing data that it will send to the SCU. For the sub-frame modes (which are all binned – see Table VI), there is added overhead as the TPG must step down the number of rows needed to get to the first row of that sub-frame, and then there will be a full row period before the data begin to flow.

To determine the center of the exposure for an IR image requires two steps. First, find the time that the readout of a row begins by using the following formula: Tstart = ITC + A(row − B) + C, where A, B and C are mode dependant and are defined in the Table VII, and ITC is the time stamp in the image header.

When this offset time is calculated, the mid-point of that line's exposure is calculated by subtracting half of the combined minimum exposure time and integration delay for that image mode.

4.1.3. *Data Flow*

The control of the instruments begins and ends with the spacecraft control unit (SCU). When power is provided to the instruments, they will initialize autonomously and within 30 s will be ready to receive commands. Commands will

TABLE VIII

Visible exposure command parameters.

Parameter	Range	Description
IMAGE_MODE	1–9	What CCD readout mode to execute – see Table IV
EXP_ID	1–99,999,999	What exposure ID to give this set of images. Must be unique or you risk overwriting a previous image
PRIORITY	1–XX	The downlink priority for images that are automatically telemetered. Lower goes earlier
DATAPATH_HW	Several	Which SCU should receive the data, and whether the images is compressed, uncompressed or both
DATAPATH_COMP	0–3	What to do with files on the compressed channel: Do not save, save to file only, save to file and send to the downlink queue
DATAPATH_UNCOMP	0–3	What to do with files on the uncompressed channel: Do not save, save to file only, save to file and send to the downlink queue
ROUTE_TO_NAV	0–1	Whether the uncompressed image will be routed to be processed by either Optical Navigation or AutoNavigation
ANAV	Several	Five parameters that contain parameters for AutoNavigation processing
LUT_SELECT	0–3	For images routed to be saved as compressed, which LUT to use.
IMAGE_COUNT	1–255	The number of images to be taken with this single image command. All images have the same parameters
INTEG_TIME	0–10,48,576, in ms	Commanded integration time
DELAY_TIME	0–16,383, in ms	Commanded time between images for multiple image exposure command[a]

[a]If only one image is commanded, this time is added to the end of the command execution and will delay the execution of the next exposure command by that much time.

come from any one of a set of 10 sequence engines in the SCU. The most common commands will be exposure commands and filter wheel commands. Commands for visible images (common to all three CCD imagers) have the parameters shown in Table VIII.

Data flow through each detector signal processing board and the IC is real time (other than the IR board offset frame storage) in that there is no buffering of the data in the instrument electronics. Once the instrument electronics have generated
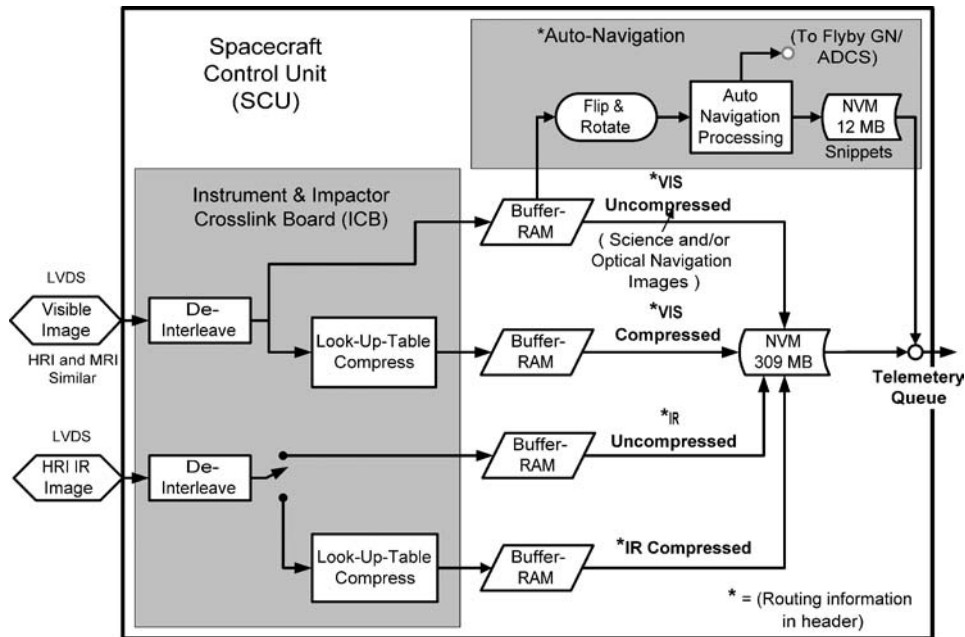
Figure 18. Data routing from the instruments to storage in the SCU, and to the downlink telemetry stream.

the image data they are transferred to the SCU *via* 12-Mbit/s LVDS interfaces. One LVDS interface is dedicated to each detector. Prior to the start of the detector readout, the same handshaking signal sent to the IC by the detector signal processing board to create the image header is sent, *via* the LVDS interface, to the Instrument and Impactor Crosslink Board (ICB) in the SCU. This enables the channel on the ICB so that it is ready to receive the forthcoming image. The IC then transmits the header, with the ITC time stamp, followed by the image data for that image. When the handshaking signal is disabled, it indicates the end of the image to the ICB.

Figure 18 shows the data path options once an image reaches the ICB. The first operation is to pull off the first 100 bytes of header data and put it aside in memory. The ICB and the instrument images software running on the SCU then snoop the header for routing and compression information to determine where the image should go. For visible images there are 27 possible permutations of routing, including to which SCU it is saved, whether it is saved as compressed, uncompressed or both, and whether it is only stored or stored and telemetered. In addition, CCD images may or may not be routed to be used by onboard AutoNavigation software. IR images can be saved only as compressed or uncompressed, not both, resulting in 18 permutations for IR images.

The first operation on the actual image data is to de-interleave the data. As the images come out of the instruments, there are four pixels converted for one CCD

at the same time. Thus, the first four pixels from the instrument to the ICB are the pixels from the outer edge of each quadrant, the next four are the next pixel from each quadrant and so forth. The ICB separates the four pixels from the CCD images into essentially four different data paths (two paths for the two IR quadrants) to reconstruct the quadrants individually in memory.

Images to be compressed are converted by means of a compression lookup table. These tables reside in EEPROM on the ICB and are simply registers with 16,384 entries, which corresponds to the maximum value of a 14-bit digital value. Each entry contains an 8-bit value that will be written to the compressed image, if the uncompressed image contains that 14-bit signal value. There are four lookup tables on each channel of the ICB – i.e. four for the HRI visible channel, four for the HRI IR channel and four for the MRI visible channel on the flyby spacecraft. A parameter in the exposure command determines which lookup table will be used for that image. The lookup table value is also captured in the image header. The lookup tables are programmable in flight to both fix any bit errors that may occur in flight and to be able to accommodate shifts in detector outputs.

The choice of lookup tables was driven largely by simplicity and timing, and also by the fact that the size of the compressed image is deterministic. The compressed image size from most compression algorithms depends strongly on the details of the image itself. With limited storage capability and requirement for high-speed imaging, larger-than-expected images could fill the DI memory before the final highest-resolution images were taken, thereby compromising the science. Visible images can be saved as both compressed and uncompressed from the same exposure command; this is to support science imaging and navigation more efficiently. The IR channel allows only compressed or uncompressed images to be stored for one imaging command, as can be seen in Figure 18.

Lookup table compression from 14 to 8 bits is not a lossless process. The tables that are currently baselined, however, make use of the fact that the photon shot noise increases as the square root of the signal. The lookup tables follow a square-root function so that at higher signal levels, the step in uncompressed signal between successive compressed values is larger. With encoding steps proportional to the square root of the signal acceptable signal-to-noise ratio can be maintained. With a lossy compression, there is always a concern that for low signal levels significant science can be compromised. In the case of Deep Impact, the concern is loss of detail in jets or ejecta from the impact. The mission team has taken several steps to collect data that reduces the impact of the loss. Since there is already uncertainty in the scene brightness of the nucleus, the image sequence includes images using several exposure times. The four tables are used to highlight different science. For images of the nucleus, two of the tables have a range that cover the full A/D converter range – 16,384 DN. For images planned to look specifically at the coma, two tables are built that span only a portion of the range of the A/D converter. With the smaller range, the low end of the table produces compressed step sizes that are one-to-one with the uncompressed step sizes. Since Tempel 1 is a low-activity

comet, the expected brightness of the coma is at maximum 1/10th of the expected surface brightness of the nucleus and 1/30th is expected. Surface brightnesses at 1/30th of nuclear signal will result in signal levels within the one-to-one range of the coma compression tables. Further, the imaging sequence includes several images that are stored on the spacecraft uncompressed.

After the ICB determines the compression routing, images are collected in software-controlled RAM buffers. When the full image has been collected in a RAM buffer, it is transferred to SCU non-volatile memory by means of direct memory access transfer. The non-volatile memory on the SCU is set up with a file system, so each image is given an unique filename. The filenames are codified with information about the instrument and detector of origin, the exposure ID and image count for that exposure ID, whether the image is compressed, and which SCU the file was collected on. Those files that are tagged for near real-time downlink are immediately sent to the telemetry queue. Each file is given a telemetry priority, and those with the highest priority will be downlinked first.

Figure 18 shows the data path to one of the two redundant SCUs. During flight, the second SCU will be powered on and will accept images to be stored in its non-volatile memory. Since the exposure commands allow routing to a single, the effective storage volume can be increased by storing images singly to one or the other SCU. However, in some cases this is not allowed, as described in Section 5.4.

5. Integration and Test

5.1. MECHANICAL INTEGRATION AND TEST

Designing a 30-cm aperture, 10.5-m focal length HRI telescope with a secondary axial magnification of 61, to operate successfully at a temperature of 140 K without a focus mechanism was quite a challenge. Therefore, we designed our test program to build confidence that the instruments would ultimately meet their performance requirements, by beginning the testing at the lowest possible component or assembly level, rather than waiting until the entire system was built, at which point fixing any problems would be costly.

One of the first tests was a cryogenic test of the figure of the HRI primary mirror. The test was conducted with an engineering model mirror with a spherical surface. In fact, the test showed that the cryogenic figure of the mirror distorted at the predicted HRI telescope flight temperature and would not meet performance requirements. A second test of a different (flight model) primary mirror showed that the EM mirror was from a flawed batch of Zerodur®, but the preliminary result illustrates the utility of early testing during a hardware development program with challenging requirements.

Next, the telescope mirrors were assembled with their structure to form the telescopes. The telescopes were tested first at room temperature for alignment

and focus. A point source, formed by a Zygo interferometer with a transmission sphere, was placed at various points across the focal plane of the HRI telescope. When this light exited the front of the telescope it was returned by a full aperture reference flat. This formed a double-pass measurement, with the beam returning to the interferometer when the reference flat was adjusted properly. The entire telescope was mounted on a stage that rotated about its long axis. With this, the alignment and focus were measured at two orientations to produce an averaged "zero-g" performance.

The MRI and ITS telescopes were aligned using a collimated beam from a 4-D Technology PhaseCam instantaneous interferometer. Five high-precision ball bearings were placed at the mechanical location of the telescope focal plane. When the collimated light was aimed into the aperture correctly, it reflected from one of the balls, returning along the same path, again forming a double-pass measurement. Focus offsets were introduced by moving the PhaseCam source toward and away from the focus of the collimator, and comparing the position of zero-power with that of a reference flat. Alignment was sensed by comparing the input angle of each ball-bearing field point to the angle of maximum return from an alignment cube fixed to the structure. The MRI and ITS alignment fixtures were also capable of rotating the telescope to determine the "zero-g" alignment and focus.

After adjustments and characterization at room temperature, the telescopes were placed in a thermal-vacuum chamber and baked at $+60\,^{\circ}$C to eliminate water in the structure. The telescopes were then measured at room temperature and at their expected operating temperatures using a collimating test system similar to the one used for the ITS and MRI room temperature alignment, and a high precision fused silica window. With this we were able to determine the effects of both moisture content and temperature on the focus and alignment of the telescopes, with only one orientation with respect to gravity.

The components of the SIM were manufactured and assembled at the same time as the telescopes. The placement of the SIM optical components was accomplished by observing well-characterized fiducial marks on the components with high-precision theodolites. The IR FPA and its radiative cooler were installed, and the SIM was placed in another thermal-vacuum chamber with the top of the SIM and radiative cooler staring at a liquid helium reservoir. The SIM was tested at its expected operating temperature of 135–137 K, as well as at 128 and 142 K. The multiple temperatures allowed us to determine the change in spectral dispersion with change in prism temperature, as well as the change in dark signal with change in the overall SIM temperature. The alignment and focus of the SIM were checked using an external test telescope that simulated the $f/35$ beam of the HRI telescope. The focus was found to be within tolerance, but the alignment was shifted slightly to the red, which could risk failure to capture the CO emission lines at 4.6 and 4.7 μm. This was corrected after the SIM was returned to room temperature by moving the final focus mirror so that the spectrum was moved toward shorter wavelengths. A second thermal-vacuum test of the SIM showed that the alignment and focus were

within requirements, and a first calibration of the spectrometer throughput was performed. During this test, a flaw in the IR FPA light shielding was discovered that we were able to fix with a simple shield near the IR FPA (also described in Section 3.3.2). The change resulted in low cost and schedule impacts to the program, again demonstrating the advantages of early testing.

After the SIM was tested, the HRI and MRI were assembled entirely and were mounted on the instrument platform. The platform was mounted on a test fixture that allowed tests with the normal to the platform up or down with respect to gravity. In this condition, alignment and focus tests were conducted on the two instruments at room temperature with the added test of checking the alignment of the two instruments relative to one another in order to meet the derived co-alignment requirement of 1 mrad. After the room temperature tests, the platform was placed in a thermal-vacuum chamber. The focus of both telescopes was tested at elevated temperature, during composite bake-out, at expected operating temperature, and the MRI focus was tested at $-30\,^{\circ}\mathrm{C}$, the expected operating temperature of the ITS at encounter. This last test was used as a surrogate for testing the focus of ITS at its operating temperature. The radiometric throughput performance of the instruments was also tested during the thermal-vacuum tests, as described in Section 5.3.

5.2. ELECTRONICS AND SOFTWARE INTEGRATION AND TEST

The testing of the instrument electronics and software also proceeded under the philosophy of testing as early as possible. Prototype microprocessors were purchased early in the program to test functionality and the software development tools. (We even found that multiplication did not work correctly in the purchased real-time operating system and wrote code to fix the problem.) Each instrument electronics board design (other than the motherboard) had a dedicated test station with custom FPGAs and LabVIEW® interfaces. These were used for board-level testing and board-level certification before integrating the flight boards in the instrument electronics. We used prototype detectors, integrated to these board-level test sets, with engineering model detector boards, to finalize the proper detector bias settings and timing patterns before the flight model electronics boards were produced. Two engineering model electronics boxes were also produced that served as safe surrogates for troubleshooting several interface and timing problems.

An Instrument Test and Operations Console (ITOC) was developed to simulate interfaces between the instrument electronics box and the spacecraft. The interfaces that were tested included commanding, telemetry, and image data flow *via* LVDS. The ITOCs were used to certify the electronics boxes, perform the flight software qualification testing, and then used during instrument level testing – taking images for calibration and alignment testing and collecting analog telemetry that allowed us to verify the conversion coefficients from raw telemetry data to engineering units.

5.3. MEASURED AND PREDICTED PERFORMANCE

5.3.1. *Focus – Over Temperature – and Expected Point Spread Function*

Focus is a concern because it directly affects the resolution that can be achieved at closest approach. The combination of telescope and instrument tests during thermal vacuum and at room temperature resulted in a good understanding of the major environmental factors that affect the alignment and focus of the instruments. For HRI the environmental factor that has the greatest effect on the focus is the telescope temperature. Figure 19 shows the relative focus offset for several telescope temperatures. The two thick horizontal lines for each temperature show the focus tolerance range over which the telescope will meet the PSF requirement. The results show that the focus (under one-g conditions) at the predicted telescope temperature is close to the optimal focus. As part of the thermal-vacuum tests, the telescopes were baked 48 h at $60\,^{\circ}$C to remove moisture before being measured at operating temperature. The effects of moisture at room temperature are also shown in the figure. This shows that elimination of water is critical to achieving the precise focus adjustment necessary to meet the system requirements.

Similar measurements made on MRI, as seen in Figure 20, show that temperature is the dominant effect, and that moisture may not need to be removed in flight to meet requirements because the effect is so small in the shorter telescopes.
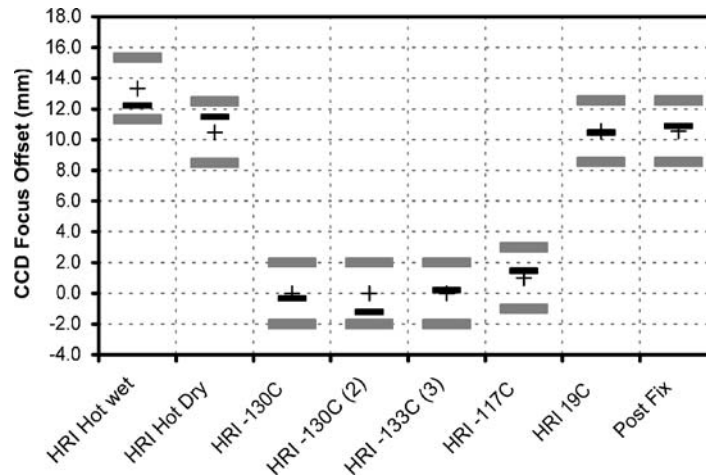

Figure 19. History of the CCD focus position during the HRI environmental test program. The format is as follows: the cross is the expected position, based on previous telescope-only tests, and the heavy gray bars are the tolerance to meet wavefront requirements. The black bar is the measured focus position. The first two measurements show the effects of moisture content on the focus an effective shift of the CCD position of 2–3 mm, which could jeopardize the focus at operating temperatures ($-130\,^{\circ}$C). All four cold measurements were within tolerance. The SIM cover was removed after the thermal-vacuum test, and a room temperature measurement shows that the focus did not shift due to this activity.
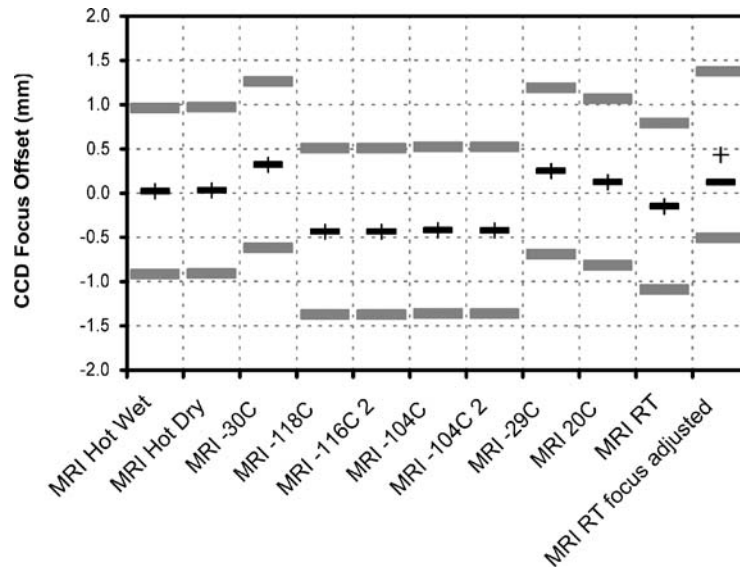
Figure 20. History of the MRI CCD telescope focus over the MRI environmental test program. The figure has the same format as Figure 19. In all cases the MRI CCD focus was in its range of focus tolerance to meet the mission requirements. A final adjustment was made to try to correct the slightly negative offset measured at cold temperatures.

The measured MRI PSF is about 1.5 pixels full width at half maximum (FWHM), which is right at the edge of that required at encounter. The HRI PSF shows a FWHM less than 2 pixels, which does meet its derived requirement of 2.5 pixels or less. The PSF was measured with a back illuminated pinhole at the focus of the collimating test set described earlier. The illumination source was a xenon flash lamp that had a few microsecond flash. This was used to reduce the effects of air turbulence and relative collimator to instrument motion. However, analysis showed that the pinhole image did jump by a few pixels from image to image. This indicates that due to the large apertures and narrow fields of view of the telescopes, these distortion effects could not be eliminated entirely, and they affected the fidelity of the measurements. Especially in the case of the HRI, the in-flight performance is expected to match or exceed what was measured. In the case of the MRI, this PSF is probably approaching the limit that can be expected due to charge diffusion in the CCD. The CCD characterization tests did not measure charge diffusion, since it was beyond the scope of the project.

5.3.2. *Alignment*

A derived requirement from the observational requirements (see Section 2) is that the boresights of the two instruments on the flyby spacecraft be co-aligned to within 1 mrad – or one-half the size of the HRI FOV, with a desire to be within 250 μrad. To measure and track this alignment, a set of high-precision alignment
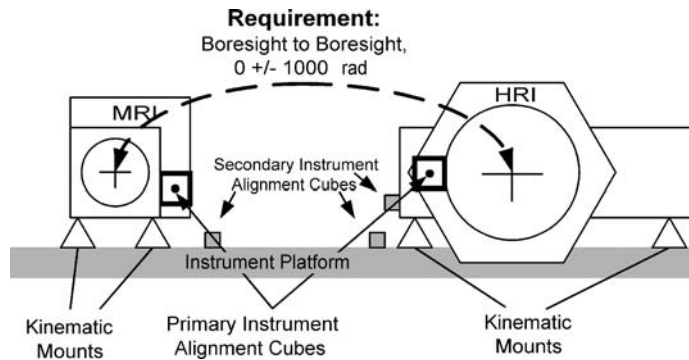
Figure 21. Placement of the instrument alignment cubes used for alignment measurements. The two alignment cubes on the instrument platform are near the kinematic mounts of the respective instruments. The second alignment cube on the HRI is on the SIM bench, whereas the primary cube on HRI is on the telescope structure.

cubes were attached to each major component on the instrument platform. Figure 21 shows their positions and the method for tracking alignment. The cubes on the MRI and HRI telescopes became surrogates for the internal boresight, and at each major I&T event the cube-to-cube alignment was measured using theodolites. There were also three main tests where this surrogate cube was measured to the actual instrument boresight; before environmental tests (vibration, and thermal vacuum), thermal-vacuum, and after environmental tests. From these measurements we have a good understanding of the effects of gravity and temperature on the alignment, and confidence that the predictions for flight are accurate.

Using two fundamental assumptions – that gravity and temperature effects are independent, and that the zero-g position is the average of those measured at the two telescope orientations that we measured at room temperature – we predicted an in-flight alignment. This result is shown in Figure 22, and ranges from exactly aligned to an offset of 60 μrad. If this is the actual performance in flight, it would allow a re-thinking of the image modes selected at the time of impact (see Klaasen), though using a smaller sub-frame does put greater reliance on the spacecraft pointing knowledge at the time of impact. The instrument-to-instrument alignment will be verified during flight calibration.

5.3.3. *Plate Scale and Targeting*

Tests using the steerable flat mirror on the collimator test station and a theodolite to measure the mirror position with high accuracy resulted in a measurement of the telescope plate scales, and a first check of telescope distortion. The effective focal length of the HRI telescope was measured, at operating temperature, to be 10.50 m, with no significant distortion in the field ($\pm 1.6\%$). The MRI telescope, also measured at operating temperature, was found to have an effective focal length
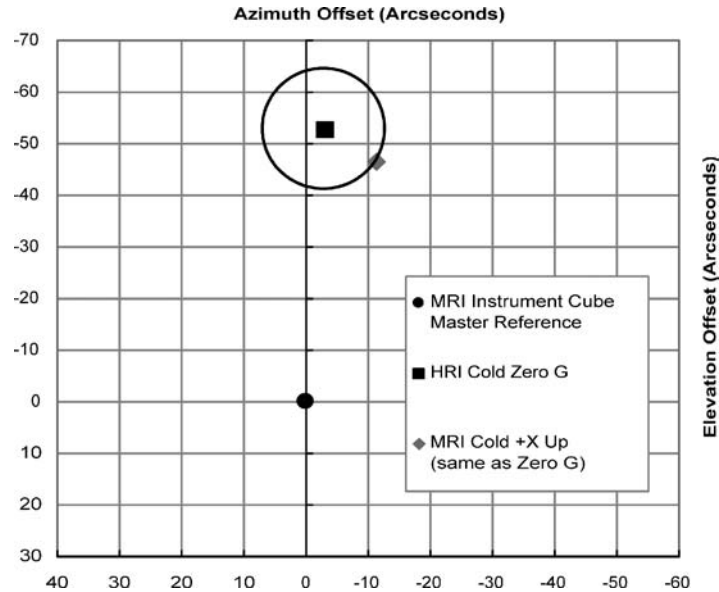
Figure 22. Results of co-alignment performance prediction, based on ground alignment measurements. All measurements are relative to the MRI Instrument Cube – the circle at (0,0). The two remaining measurements are the boresight of HRI and MRI relative to that measurement. The MRI boresight measurement is stable for both orientation of the instrument with respect to gravity. The error circle is 60 μrad in radius based on the scatter in the HRI measurements.

of 2.10 m, again with no significant distortion. The ITS focal length was not measured at operating temperature, but its room temperature focal length was also 2.10 m with no significant distortion. Data were taken that imaged a test target rastered across the field of view of each instruments, but has yet to be analyzed. This test and planned observations of open clusters during the mission cruise will further define any distortions in the focal plane and aid in the interpretation of both the navigation data and the scientific interpretation of the effects of the impact event.

5.3.4. *System Noise and Offset*
Images taken during thermal-vacuum testing of the instrument platform and flight system show that the CCD read noise is 1 DN, which allows the system to easily meet science imaging requirements. The LUT compression system applies the same selected LUT to all quadrants on a CCD image, or to both halves of an IR image. Thus, if one quadrant has an offset value that is significantly different than the others, it can adversely affect the possible SNR of other quadrants of compressed images. For example, if one quadrant of a CCD system has an offset that is 100 DN lower than the three others, over one-third of the LUT would be used up accommodating the one low quadrant. The three other quadrants would only have 155 levels above
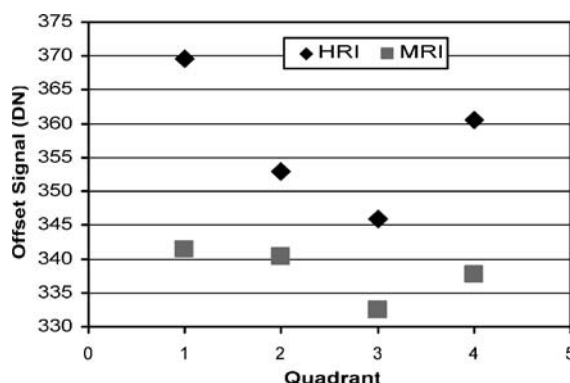
Figure 23. HRI and MRI CCD serial overclocked average signal levels. There is a nearly 23 DN difference between quadrants 1 and 3 in HRI. The spread in MRI is less than 10 DN.

their offset, and therefore would have their dynamic range significantly reduced. Therefore, a derived goal for the system was to have the offset of the quadrants within 15 DN of one another on all systems but the ITS.

Figure 23 shows the CCD offsets for HRI and MRI with the CCDs near their operating temperatures. The HRI shows nearly 20 DN difference from the highest to the lowest offset level. The MRI shows less than 10 DN from the highest to lowest level.

The scientific modes of the IR detector perform a subtraction of the reset levels of each pixel from the integrated values. Thus the signal left in the imaging area of the detector is the dark signal, which is a combination of the detector dark current, and the background IR radiation generated by components on the SIM bench. The detector does have five rows of reference pixels around the edge of the detector that are not connected to the HgCdTe substrate. In the DI three of these edges are available in full-frame images. of the images that are collected on DI. While the expected performance is to all be at a signal level of zero after the subtraction, the reality is that there is a slight variation across columns. While the source of this profile is not explained, the condition is stable over a wide range of conditions, and can be used as a quick diagnostic.

The two tests of the IR spectrometer at the SIM level were by far the best tests of the IR detector during the entire development program. In this case, the detector reached an operating temperature of 85 K, close to the predicted flight temperature. These tests were used to determine both a bad pixel map of the detector (see Section 5.3.7) and the dark signal performance of the spectrometer. Figure 24 shows the results of an analysis of dark signal over a wide range of temperature conditions. The figure shows a good Arrhenius curve of dark current versus temperature, after the prism temperature has been subtracted. This indicates that a large portion of the dark signal results from the prisms which are in the light path, and have a higher emissivity than does the bare aluminum surfaces of the mirror.
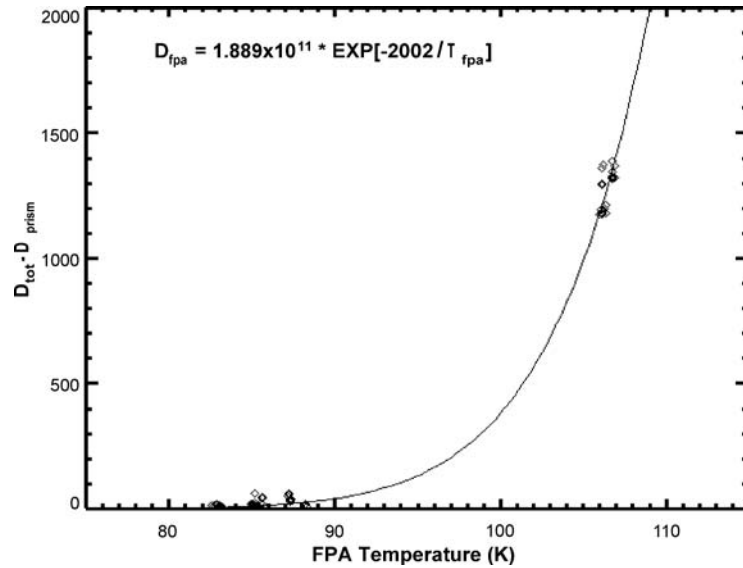
Figure 24. Dark signal for the HRI IR FPA. This plot shows the relationship between dark signal and the FPA temperature. The effect of prism temperature has been removed. The signal is that which is measured during a 2.86-s exposure time, the minimum for IR imaging modes 1 and 4.

5.3.5. *System Throughput in the Visible and IR, and Expected SNR at Encounter*
A major driver in the instrument resolution at the encounter is the length of the exposure time. A shorter exposure reduces the time that the imager is subjected to jitter of the spacecraft platform. A measurement of the instrument throughput will allow for a better prediction of the needed exposure times and thus an estimate of the resolution at closest approach.

Part of the calibration was to image a calibrated integrating sphere for both flatfield and throughput measurements. A forward model of the instruments, using all the measured components, was used to predict the throughput from each instrument. The model and the measured signal compared favorably. With the good comparison, the forward model can then be used to produce a calibration factor for all filters on both HRI and MRI, as shown in Figure 25. The calibration factors are calculated for a flat spectrum with unit flux of units μ W/(cm^2 sr^2 nm^1). Also shown in the figure are the same calibration factors for the Multi-Spectral Imager used on the Near Earth Asteroid Rendezvous (NEAR) mission as reported by Hawkins *et al.* (1997). The model can also be used to predict the signals that are expected at the encounter. The predicted signal rates for each filter of the HRI imager are shown in Table X. This model includes the effects of coma, and the calculation only include the SNR of the surface features. In this case, the coma was assumed to be one-third of the nucleus signal, which is conservative for Tempel 1. The mission requirement is that the crater be imaged with an SNR of 70 at closest approach. The table, along with the noise measurements of the CCD system and an estimate of the coma signal,

TABLE IX

Predicted signal rates for HRI at comet Tempel 1, and exposure times to meet SNR.

| Filter	Rate (DN/s)	Rate (electrons/s)	SNR						
			10	30	50	70	100	150	250
1	3114.5	87,829	0.004	0.019	0.044	**0.080**	0.158	0.347	0.953
2	398.9	11,249	0.032	0.145	0.342	0.628	1.233	2.712	7.443
3	688.5	19,415	0.018	0.084	0.198	0.364	0.715	1.572	4.312
4	78.1	2,203	0.162	0.742	1.744	3.208	6.296	13.85	38.00
5	214.4	6,045	0.059	0.270	0.636	1.169	2.295	5.047	13.85
6	3110.2	87,707	0.004	0.019	0.044	0.081	0.158	0.348	0.955
7	505.2	14,247	0.025	0.115	0.270	0.496	0.974	2.142	5.876
8	303.7	8,564	0.042	0.191	0.449	0.825	1.620	3.563	9.775
9	666.2	18,787	0.019	0.087	0.205	0.376	0.738	1.624	4.456
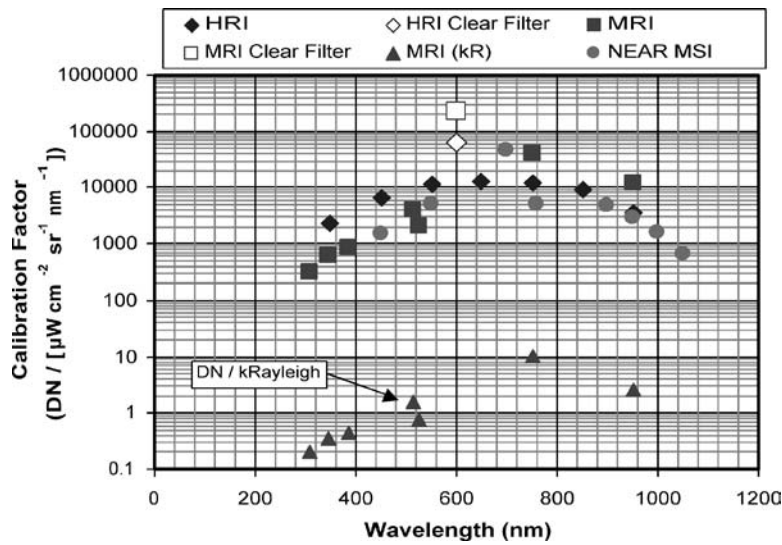
Figure 25. Calibration factors calculated for HRI and MRI for a 1-s exposure. Also shown are calibration factors for the NEAR MSI camera.

shows that exposure times of 0.080 s will produce a surface SNR of 70 or greater for images using a clear filter (e.g. Filter 1).

For MRI and ITS, similar tables are produced and these are used to set exposure times for the image sequence. The gas-filter observation of the coma take significant exposure times, and may be accumulated from a number of shorter exposures. With low relative readout noise this is possible.
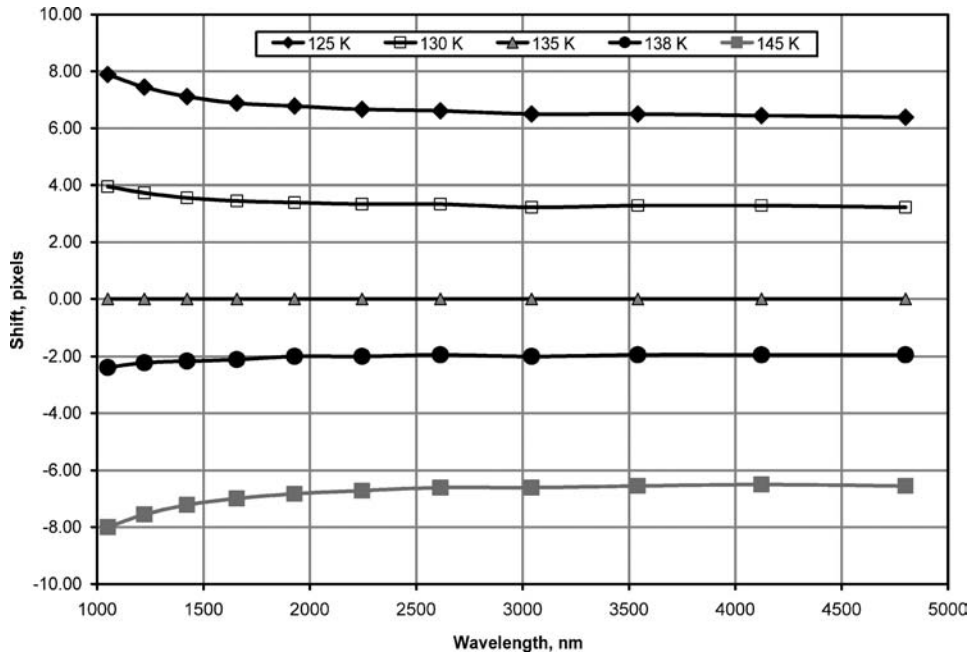
Figure 26. Wavelength shift of the IR spectrometer vs. prism temperature. The shift in center wavelength from the nominal center wavelength at a prism temperature of 135 K is plotted for each column for several cases. The wavelength shift with prism temperature is largely the same, 0.6 pixels/degree, over most of the spectrum. Below 2 μm, however, the rate of shift is wavelength dependant.

5.3.6. *IR Spectrometer Alignment, Wavelength Map and Spectral Resolution*
Section 5.1 describes the testing of the IR spectrometer at the SIM level. During these tests, the SIM optical bench was adjusted to three temperatures, along with the prisms. This allowed a measurement of the change in dispersion of the prisms with temperature. Using spectral lines of Kr, Ar, CO, and NH$_4$, as well as the ever-present CO$_2$ and H$_2$O when observing sources outside the chamber, a wavelength map was produced for each bench temperature. Figure 26 shows the wavelength maps at the three test temperatures. The wavelength shifts were compared to empirical formulae produced by Tropf (1995) and found to match closely.

With the wavelength mapped, the geometric spectral resolution is easily calculated. Figure 27 shows the spectral resolution at 137 K, the nominal flight temperature. The minimum geometric resolution is 216, which meets the required minimum of 200. Measurements of the line width for spectral lines of Kr and Ar that are known to be singlets shows that line widths are 1–1.1 binned pixels wide. At worst case the spectral resolution is 196.

As with any imaging spectrometer, the spectral lines show some curvature, or "smile" on the focal plane. The slit misalignment to the detector is less than one pixel across the 512 rows.
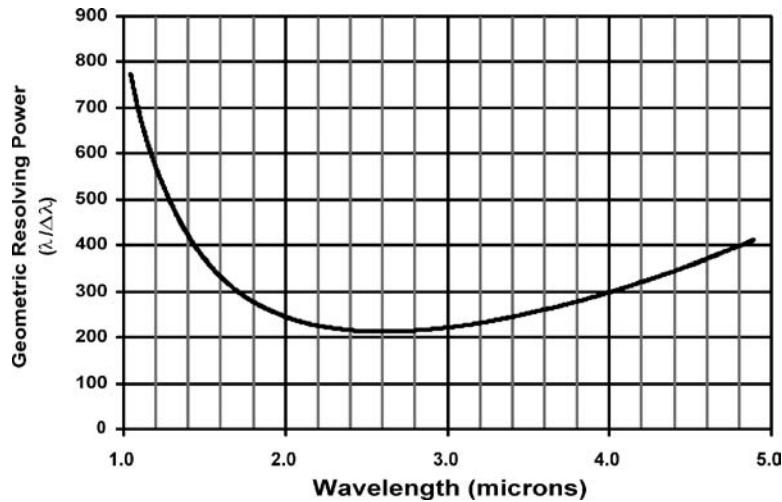
Figure 27. Geometric resolving power for the HRI IR spectrometer. The resolution is shown for the optical bench at an operating temperature of 137 K.

5.3.7. *Detector Bad Pixel Maps*

Interpreting the data requires an understanding of which pixels are inoperable, or have performance significantly less than the average pixel. Data from several tests could be used to make this determination.

The IR detector showed about 3.5% inoperable pixels on an initial analysis. The criterion used to determine an inoperable pixel was that it was greater than four standard deviations from the mean signal. Many of the pixels that have been initially categorized as inoperable may still have reduced performance, but information may be recovered. This is the subject of future work in analyzing the ground calibration data.

The CCDs showed impressively low numbers of bad pixels. The CCD in the HRI has one pixel that at room temperature is considered a "hot" pixel, and leaves an obvious trail of charge when operated. However, when the CCD is cooled below $-40\,^{\circ}$C, the pixel seems to behave normally.

Figure 28 shows the boundary between the two image areas (see figure CCD-1 in Section 3.3.1). Because the readout circuits of the two halves are electrically isolated, there is additional traces at this boundary that reduce the effective collection area of the edge pixels. The figure was taken while the HRI was looking at an integrating sphere for flat-field testing. The signal in the two edge rows is consistently 15.5% less than that of the main region. There is a slight color variation on the order of 2%.

5.4. OPERATIONAL CONSIDERATIONS

There are necessarily limitations on how the instruments are commanded and controlled, and how they interface with the spacecraft. Some of the limitations were
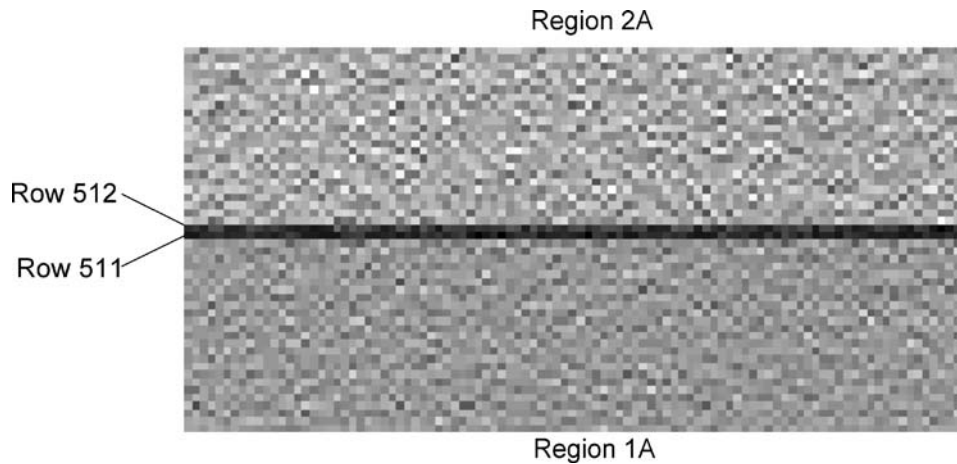
Figure 28. Close-up of a CCD flat field image at the boundary between the two imaging regions. The two rows that are reduced are due to extra traces in the CCD readout required to maintain independence between the two halves of the CCD. Regions 1A and 2A refer to the regions shown in Figure 9.

planned to reduce complexity and maintain cost, while others were discovered during interface testing with the spacecraft.

5.4.1. *IR Exposure Commands*
Two limitations, that were not planned, have to do with how the IR detector exposure commands are issued. Both have to do with interface issues with the ICB. First, there is a minimum commanded exposure time of 250 ms for IR mode 4 (interleaved, unbinned) images. This is required to ensure that the IR channel of the ICB is re-initialized. Second, IR images commanded to only one SCU will lock up the IR channel of the ICB in the other SCU. In other words, commanding IR images to be stored only on SCU-A will put the IR channel of the ICB in SCU-B into an indefinite "busy" state. This limitation is avoided by sending IR images to both SCUs in each command, which is the new baseline for the encounter imaging sequence.

5.4.2. *Data Rates and Limitations*
To support the unique mission scenario, the detector readout rates were set at 187,500 pixels per second per quadrant, and all three detectors from the flyby spacecraft may be transmitting data simultaneously. This scenario – such a high data rate from three instruments – is unique to planetary missions, to the knowledge of the authors. The ICB can receive the data at this rate from all three detectors as well, but once the data are being written to the SCU, all three detectors are attempting to access the same non-volatile memory simultaneously. Effectively, the data storage rate has been found to be 1.4 MB/s. During the 13 min from impact to closest approach, running at this rate would result in over 1 GB of image data being produced. That much storage is not available, so on average, the storage rate

to non-volatile memory is not a limitation. The last few images are the highest resolution and therefore of the highest importance to the surface science goal of the mission and are taken in rapid succession. Early testing showed that short bursts of imaging at rates slightly above 1.4 MB/s resulted in one to six images being lost. Further adjustments to the imaging sequence and the management of the file system have resulted in subsequent tests storing all commanded images.

6. Conclusions

The Deep Impact instruments will collect the images from the first active experiment on a comet nucleus. They were designed based on the needs and constraints of the Deep Impact mission. Other than the de-scopes early in the program, required to meet budget constraints, the instrument team has produced instruments that match or exceed the desired performance envisioned at the beginning of the project. The testing showed that the ground performance will meet all the requirements. The ability to recover from anomalies during integration and test was enhanced by testing at the lowest assembly level as possible.

Acknowledgements

References

A'Hearn, M. F.: 2005, *Space Sci. Rev.*, this issue.
Ball Aerospace & Technologies Corporation: 2002, *561177 Instrument B-Specification*, Revision D.
Hawkins, S. E., Darlington, E. H., Murchie, S. L., Peacock, K., Harris, T. J., Hersman, C. B., *et al.*: 1997, *Space Sci. Rev.* **82**, 31.
Klaasen, K. P., Carcich, B., Carcich, G., and Grayzeck, E. J.: 2005, *Space Sci. Rev.*, this issue.
Richardson, J., Melosh, H. J., Artemeiva, N. A., and Pierazzo, E.: 2005, *Space Sci. Rev.*, this issue.
Schultz, *et al.*: 2005, *Space Sci. Rev.*, this issue.
Tropf, W. J.: 1995, *Optical Eng.* **34**, 1369.
Jet Propulsion Laboratory: 2004, *Mission, Science, and Systems Requirements Document*, JPL D-16496, Revision C.